IEEE Access
Multidisciplinary ⋮ Rapid Review ⋮ Open Access Journal

Received 24 October 2023, accepted 12 November 2023, date of publication 20 November 2023,
date of current version 27 November 2023.

Digital Object Identifier 10.1109/ACCESS.2023.3334637

RESEARCH ARTICLE

Flexible Free-Space Optical CDMA Networks

MARÍA ÁLVAREZ-ROA[1], CARMEN ÁLVAREZ-ROA[1], THIAGO R. RADDO[2], MIGUEL CASTILLO-VÁZQUEZ[2], CARMEN CASTILLO-VÁZQUEZ[2], BEN-HUR V. BORGES[3], IDELFONSO TAFUR MONROY[1], (Senior Member, IEEE), AND ANTONIO JURADO-NAVAS[2], (Member, IEEE)

[1]Eindhoven University of Technology, 5600 MB Eindhoven, The Netherlands
[2]Communications and Signal Processing Laboratory, Telecommunication Research Institute (TELMA), University of Malaga, 29010 Málaga, Spain
[3]Department of Electrical and Computer Engineering, University of São Paulo, São Carlos 13566-590, Brazil

Corresponding author: Antonio Jurado-Navas (navas@ic.uma.es)

This work was supported in part by the Ministerio de Ciencia, Innovación y Universidades under Grant PID2019-107792GB-I00; in part by the Fundação de Apoio à Pesquisa do Estado de São Paulo under Grant 2013/07276-1 and Grant 2021/06121-0; and in part by the Dutch Ministry of Economic Affairs and Climate Policy (EZK), as a part of the Quantum Delta Netherlands (NL) Programme.

ABSTRACT In this paper, we propose a novel hybrid network solution using optical code-division multiple-access and free-space optics (OCDMA-FSO) to support multiple data rates and quality-of-service according to user requirements. The proposed OCDMA-FSO network classifies users into diverse classes based on their requirements and allows for signal transmission in a fully asynchronous manner. The new hybrid network employs 2-D OCDMA codes as well as a variable aperture FSO receiver together with an equal gain combining (EGC) technique. We derive completely new analytical formalisms to evaluate the network performance in terms of average bit error rate (ABER), outage probability, effective data rate during outages, and ergodic capacity. The derived ABER expressions are validated via Monte-Carlo simulations. These new analytical formalisms are derived considering several atmospheric turbulence conditions such as uncorrelated, totally correlated, and partially correlated turbulence. To model this atmospheric turbulence, we derive the gamma-gamma (GG) distribution, which allows us to consider both the scintillation effect and the EGC technique. Finally, we carry out a comprehensive performance evaluation of the proposed hybrid network. Analytical results show that as the number of FSO receiver apertures increases, there is an improvement in overall performance levels. However, the ergodic capacity exhibits minimal improvement even as the number of FSO receiver apertures increases, regardless of the user requirements and turbulence conditions. The proposed network is a potential solution for scenarios that demand flexibility in bandwidth and data rate allocation.

INDEX TERMS FSO, OCDMA, BER, outage probability, ergodic capacity, turbulence, spatial diversity.

I. INTRODUCTION

The innate need to exchange information has motivated individuals to explore a variety of means and methods to achieve these goals. Amongst several current network technologies, passive optical network (PON) has emerged as the dominant solution, reaching into end users' homes and business premises, enabling a new range of broadband services to be delivered [1], [2]. The main reason for the success of PON is its inherent ability to share the underlying network resources among the users. In addition, the judicious allocation of PON resources is becoming of paramount importance to support the growth in traffic demands in the upcoming years.

Several different technologies have been developed to support the traffic demands of today's society. A high-capacity PON based on optical code-division multiple-access (OCDMA) technology can be deployed [3], [4], [5]. Such a technology enables several users to transmit data concurrently, and in a fully asynchronous manner by means of a unique code assigned to each user. OCDMA offers numerous benefits to the network, including asyn-

The associate editor coordinating the review of this manuscript and approving it for publication was Daniel Augusto Ribeiro Chaves.

chronous transmission, versatile bandwidth allocation, and enhanced security compared to its counterparts. Compared to traditional multiplexing techniques such as time-division or wavelength-division multiplexing, CDMA offers enhanced flexibility in allocating bandwidth. It is also a statistical multiplexing technique that supports multiple data rate transmissions at the physical layer. Whilst OCDMA-based PON may be the optimal technology for future access networks, its deployment is restricted by geographical challenges, limited optical fiber deployment, and site access rights limitations, among others [4], [6].

An alternative approach to tackling these challenges relies on free-space optical (FSO) technology, which has recently emerged as an alluring and economical strategy to offer secure, high-speed transmission in regions where fiber infrastructure is inadequate or absent. FSO communications benefit from unregulated bandwidth available in optical frequencies, enabling data rates as high as those in PON [7], [8], [9]. Consequently, successful implementation of FSO systems occurs in not only access networks but also cellular fronthaul [4] and backhaul [10], along with various other intriguing scenarios [8], [11].

As societal needs evolve, next-generation networks such as 6G will require higher capacity, data rates, and lower latency, to name but a few [12], [13]. In the future, networks will support similar uplink and downlink capabilities, particularly in terms of bandwidth. Combining FSO and OCDMA technologies delivers a practical solution for deploying access networks in remote geographical areas, where fiber infrastructure is absent [14]. Furthermore, hybrid OCDMA-FSO systems have the ability to enable next-generation networking capabilities, including increased bandwidth, higher data rates, and full symmetrical operation. The fact that dedicated optical signals are used for the users allows for statistical multiplexing gain, which is desirable when bursty traffic occurs. Additionally, OCDMA allows users to access and transmit data asynchronously in the network. Similarly, FSO provides asynchronous data transmission and support for bursty traffic. This effective solution, employing OCDMA-FSO technology, achieves high-speed and secure transmissions while retaining the asynchronous transmission feature of both technologies.

An OCDMA-FSO solution was investigated in [14]. However, it relies on a fixed bandwidth allocation scheme, lacks quality-of-service (QoS) capability, and does not support multiple data rates, resulting in all users transmitting at the same rate and QoS. An OCDMA network with support to multiple data rates was addressed in [3]. However, the study only concentrated on optical fiber networks and did not encompass FSO technologies. In contrast, [15] evaluates the performance of an OCDMA network in varying weather conditions and atmospheric turbulence levels. The network uses a fixed bandwidth allocation scheme without QoS capability or support for multiple data rates. Finally, [16] presents an experimental demonstration of an OCDMA-FSO network with a fixed bandwidth allocation and without QoS provision.

A random diagonal OCDMA code set combined with polarization-division multiplexing was used in an FSO network in [17]. This network architecture requires precise management of signal polarization, presenting a significant challenge for practical application. On the one hand, enhanced double-weight, modified double-weight, and multi-diagonal codes are implemented in a hybrid network [18], with the aid of machine learning to differentiate and categorize distinct signal codes. Nonetheless, the network has the capacity to support only a limited number of simultaneous users. On the other hand, a 3-D code with zero cross-correlation is proposed in [19]. Despite displaying noteworthy levels of performance, implementation of such a code in an actual networking scenario would be challenging. Alternatively, diagonal permutation shift codes are used to encode the different polarization signals of an OCDMA network based on FSO in [20]. Unfortunately, the latter can only accommodate a limited number of users in the system. In addition, enhanced double-weight codes are used together with orbital angular momentum signals in an FSO network [21]. However, the network does not support different data rates and the number of users in the system is small due to the current limitations of orbital angular momentum technology.

In this paper, we propose a new network architecture based on OCDMA-FSO that supports resource allocation based on user requirements. Users in the network are classified into different classes based on their data rate and quality-of-service (QoS) requirements. The proposed network uses a 2-D multiweight multilength optical orthogonal code (MWML-OOC), and a variable aperture FSO receiver, alongside an equal gain combining (EGC) technique. We derive new analytical formalisms to assess the network performance, concerning the average bit error rate (ABER), outage probability, effective data rate during outages, and ergodic capacity. The newly derived ABER expressions are validated via Monte-Carlo simulations. The analytical formalisms are derived considering FSO scenarios under different atmospheric turbulence, including uncorrelated, totally correlated, and partially correlated turbulence. The gamma-gamma (GG) distribution, widely employed by the scientific community, is implemented to model the atmospheric turbulence, enabling the accounting of both the scintillation effect and the EGC technique on the spatial diversity-based FSO receiver. To accomplish this, the probability density function (PDF) of the GG model, which represents the irradiance fluctuation associated to different turbulence scenarios, is derived. Then, we perform an extensive assessment of the proposed hybrid network, encompassing a variety of factors, including the length of the FSO link, apertures of the FSO receiver, and levels of turbulence, ranging from weak, moderate, and strong, among others. The results of the analysis show that (i) class-1 users exhibit superior overall performance, (ii) the overall performance levels improve with increasing

number of FSO receiver apertures, (iii) strong turbulence regimes significantly reduce performance levels, and (iv) the ergodic capacity shows a slight improvement as the number of FSO receiver apertures increases, regardless of the user class and turbulence regime. The proposed network is a potential solution for scenarios where flexible allocation of bandwidth and data rates are key system requirements.

This paper is organized as follows. Section II lays out the hybrid network architecture as well as defines the system model concepts that will be used later in the development of the mathematical formalisms. Section III presents the mathematical model that characterizes the behavior of the received irradiance signal at the FSO receiver. Section IV presents the mathematical procedure used to derive the ABER and discusses its results. Section V develops various figure-of-merits such as outage probability, effective transmission rate in outage conditions, and the ergodic capacity. Section V also shows and discusses the results for these metrics. Lastly, Section VI presents some concluding remarks focusing on the main results and new insights.

II. FLEXIBLE OCDMA-FSO NETWORK ARCHITECTURE

In this section, the architecture of the hybrid network that supports flexible bandwidth allocation and multiservice transmissions is described. The flexible OCDMA-FSO network proposed here is arranged in a star topology connecting all users to the multiple access channel via optical fibers, where each user has a transmitter and receiver as illustrated in Fig. 1. The network consists of S-class users sharing the same optical medium, where users are divided into classes according to their required QoS and transmission rates [3].

In the OCDMA-FSO network, each user class $s \in \{1, 2, \ldots, S\}$ has its users' data rate defined according to its own code length in a way that high rate users have smaller code length, and low rate users have longer code length such that $L_1 < L_2 < \cdots < L_s < \cdots < L_S$, and $L_s = T_s/T_c$, where T_s and T_c are the bit and chip period, respectively. Also, the network supports QoS transmission through specific code weights W_s where the larger the code weight, the higher the QoS supported; where the code weight is associated with the number of non-zero elements in a code. Without any loss of generality, it is assumed that the desired user is the first user in the desired class denoted as s'. The total number of users in the network is $U = \sum_{s=1}^{S} U_s$, where U_s is the number of class$-s$ users. The user data bits are on-off keying (OOK) modulated and each user transmits using an exclusive code [22]. The 2-D MWML-OOC used here is constructed based on both the 1-D MWML-OOC for time-spreading allocation of a data bit, and on the prime code for wavelength-spreading [22]. The code set is characterized by the quadruple (W, L, λ_a, λ_c) with unipolar (0, 1) sequences, where W, L, λ_a, and λ_c are the code weight, code length, maximum nonzero shift autocorrelation, and maximum cross-correlation. Normally, a code sequence has L chips and the temporal distance among the chips can be any integer number in {1, 2,..., L - 1}. The total number of wavelengths in a code set is a prime number. Wavelength permutations are carried out over the Galois field in order to fill up a number of W chip slots. The code set has good correlation properties with auto-correlation and cross-relation values bounded by one at most. The cardinality of the code is $C = U + \sum_{s=1}^{S} U_s$. The 2D MWML-OOC encodes the data bit in both time and wavelength domains in a flexible way such as the weight and length of code sequences can be chosen arbitrarily. Consequently, this allows for (i) generation of different code lengths; (ii) a large pool of available codes, and (iii) support for flexible data rates and differentiated-QoS while satisfying good correlation properties. Further details about the code construction can be found in [22]. The OCDMA codes can be implemented in practice by using optical delay lines and wavelength-division multiplexing devices such as arrayed waveguide grating [23]. Sequentially, the optical signal is encoded by the OCDMA encoder. Then, the passive star coupler combines the output signals of all transmitters and provides access to the fiber channel. We consider that all optical fiber non-idealities are appropriately compensated while ignoring other deleterious sources [24]. Additional noise sources such as shot, thermal, and dark current noises will be considered and published elsewhere. Interested readers should refer to [25] and [26] for FSO system analysis with additional receiver noises. However, the simple superposition of users' signals in the star coupler produces multiple-access interference (MAI), which is delivered to each user by the optical splitter [27] (at the fiber channel receiver side). Next, the combined signal is transmitted through the FSO channel, where signal fading may occur due to atmospheric turbulence scintillation. The latter can affect both signal intensity and phase and consequently deteriorate the transmitted signal [28], [29]. However, signal phase is not an issue in incoherent networks since only the signal intensity is encoded [3], [27]. Conversely, the FSO receiver, which employs an EGC spatial diversity technique using up to four aperture collecting lenses [29], collects the transmitted signal and a passive star splitter delivers the signals to each user receiver. Finally, the OCDMA decoder removes the temporal and wavelength translation previously introduced in the transmitter side. Thus, the decoded signal is sent to a photodetector and subsequently to an OOK demodulator where the output signal is integrated and compared to a threshold level to retrieve the original binary data. Interested readers can found further details about the OCDMA encoding/decoding process in [14].

A. SYSTEM MODEL

The flexible OCDMA-FSO network uses OOK modulation along with direct detection scheme. Thus, the normalized received optical irradiance, I, acts as a random variable since it is affected by the effect of the turbulence-induced fading. The received optical power in the OCDMA receiver followed by the FSO link suffers from a fluctuation in the

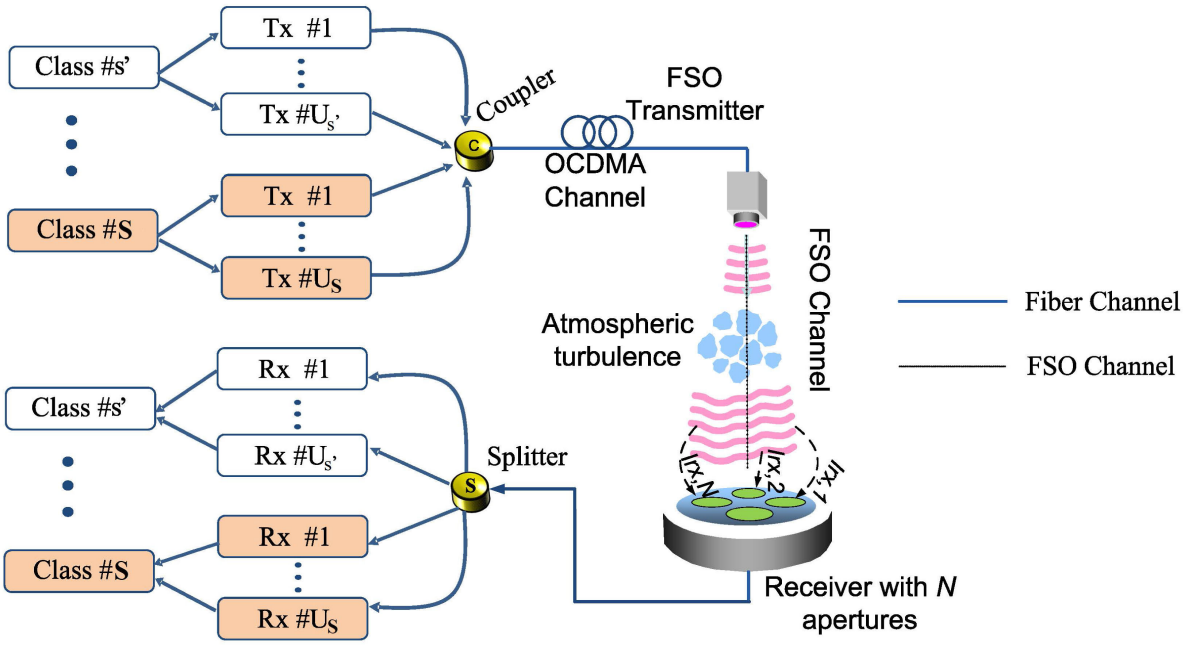

FIGURE 1. Architecture of the flexible OCDMA-FSO network connecting all users in a star topology via optical fibers and a FSO link. Tx: transmitter Rx: Receiver.

signal intensity due to atmospheric turbulence, MAI, and shot noise caused by the ambient light. In this case, the shot noise can be modeled to high accuracy as an additive white Gaussian noise (AWGN). Then, the receiver collects a portion of the transmitted optical field (measured in its responsivity parameter), which is focused onto a photodetector surface. Accordingly, the instant photocurrent at the detector output in the OCDMA receiver followed by the FSO channel is given by

$$y(t) = R \cdot I(P_T(t) + I_1) + N(t), \tag{1}$$

where I represents the normalized turbulence-induced fading coefficient, i.e., the effect of the intensity fluctuations on the transmitted signal. It is worth mentioning that I is a random variable with statistical average $E[I] = 1$, which includes the refractive and diffractive effects of the atmospheric turbulence cells. R is the detector responsivity assumed here as 1, and $P_T(t)$ is the transmitted optical power. $P_T(t)$ has a deterministic value, which includes the atmospheric loss. In addition, I_1 represents the total MAI (in units of power) given by the sum of the interferences from all users, and $N(t)$ is the detector noise current at the receiver, which is assumed as AWGN with zero mean and variance σ_N^2. Under the absence of turbulence, the signal-to-interference-plus-noise ratio (SNIR) of the OCDMA channel at the receiver for each user class-$s \in \{1, 2, \ldots, S\}$ is expressed as

$$\gamma_{s0} = \frac{W_{s'}^2}{\sigma^2 + \sigma_{N'}^2}, \tag{2}$$

where $W_{s'}$ is the code weight, $\sigma_{N'}^2$ is the AWGN generated solely in the OCDMA channel, and σ^2 represents the MAI variance. Next, and considering now the effect of the atmospheric turbulence, since the MAI term is affected by I, $\sigma^2(I)$, then the SNIR in (2) can be approximated by averaging the noises over atmospheric turbulence in the way proposed in [30] and [31] as

$$\gamma_{s0}(I) \approx \frac{W_{s'}^2}{< \sigma^2(I) > + < \sigma_N^2 >} \tag{3}$$

where $< \cdot >$ is the average over turbulence, and where σ_N^2 includes, not only the AWGN in the OCDMA channel, $\sigma_{N'}^2$, but also other sources affecting the FSO link, with the shot noise ($\sigma_{N_{sn}}^2$) being the most important one. In this respect, we assume a shot noise limited system as in [32] and thus, we have ignored background illumination, circuit, and thermal noise, so $\sigma_N^2 = \sigma_{N'}^2 + \sigma_{N_{sn}}^2$, where the received power fluctuations in the signal induced by the atmospheric turbulence become, in addition, a contributor to the detector shot noise. Furthermore, $< \sigma^2(I) >= \sigma^2 = (U-1)\mathcal{P}(1-\mathcal{P}) \gg \sigma_{N'}^2$ since $< I >= 1$ was assumed, where U represents the total number of simultaneous users, and $\mathcal{P}$ denotes the multirate probability of interference between the desired user and an interfering user defined as

$$\mathcal{P} = \sum_{s=1}^{S} \frac{N_s p_{ss'}}{(U-1)}. \tag{4}$$

N_s is the number of interfering users in class-s, $p_{ss'}$ is the total probability of interference caused by a code of class s on a

code of class s', i.e. $p_{ss'} = W_s W_{s'}/(2L_s F)$; where L_s is the code length associated to class-s, and F is the total number of available wavelengths. Next, the shot noise as an AWGN is taken into account, due to the ambient light affecting the transmission in the FSO link. Then, from (1), the electrical SNIR associated to the user class-s at the receiver can be directly obtained as in [33, Eq. (1)] as follows

$$\gamma_s = (RI)^2 \gamma_{s0}(I) = \gamma_0 I^2, \tag{5}$$

where $\gamma_{s0}(I)$ is the approximation for the received SNIR for class-s in the absence of atmospheric turbulence, as defined in (3), with $\gamma_0 = R^2 \gamma_{s0}(I)$. We assume $R = 1$ and, consequently, $\gamma_0 = \gamma_{s0}(I)$ for the sake of simplicity.

III. SPATIAL DIVERSITY: CORRELATED SCINTILLATIONS

Even though the flexible OCDMA-FSO network has several advantages such as wise use of the available bandwidth, it also faces channel impairments. Atmospheric path-loss, turbulence-induced fading (usually called scintillation), and blockage are examples of such impairments that can limit up to a few kilometers the propagation path length [34]. Nevertheless, the most deleterious atmospheric effect is produced by random changes of the medium refractive index along the propagation path. This effect known as atmospheric turbulence leads to the appearance of random fading intervals in the received optical irradiance. This performance degradation is deduced from the probability density function (PDF) of the irradiance. The gamma-gamma (GG) model [35] has been widely used to model the turbulence induced fading in FSO links due to its mathematical tractability, which considers the optical scintillation as a conditional random process [28], [32], [35], [36].

An attractive solution to mitigate the degrading effects of atmospheric scintillation is the use of spatial diversity reception [37], [38]. Spatial diversity in direct detection systems is an alternative to large-aperture receivers as it is based on an array of small aperture receivers. The small apertures are spatially separated by a sufficient distance so that they are statistically independent. Nonetheless, for this assumption to hold true, the spacing between receivers should be greater than the fading correlation length.

The performance evaluation of these scenarios requires the correlation among sequences of scintillation to be incorporated into the GG PDF [29] in such a way that the received optical irradiance can be expressed as a sum of individual contributions received by each single receiver aperture. It is assumed that the same large eddies affect the signal received by the N receiver apertures. Hence, the large-scale scintillation-component is a common contribution for all of them, i.e., $X_i = X, \forall i = 1 \ldots N$, with X following a gamma distribution with parameters α_x and $1/\alpha_x$. In contrast, the diffractive small-scale turbulence effect Y_i depends on each aperture, although it is assumed that each Y_i is identically distributed and characterized by $\alpha_i = \alpha$ and $\beta_i = \beta = 1/(N\alpha)$ as a normalized optical irradiance, $I = X \sum_{i=1}^{N} Y_i = XV$ is considered. Accordingly, the irradiance GG PDF, $f_I(I)$, consists of a double stochastic scintillation theory, which assumes that small scale irradiance fluctuations are modulated by large-scale irradiance fluctuations of the propagating wave [29]. Then, the correlation matrix of the photodetector with up to four apertures following an exponential correlation model, a lineal equidistant photodetectors array [39], can be built as

$$C_Y = \begin{pmatrix} 1 & \rho_1 & \rho_2 & \rho_3 \\ \rho_1 & 1 & \rho_1 & \rho_2 \\ \rho_2 & \rho_1 & 1 & \rho_1 \\ \rho_3 & \rho_2 & \rho_1 & 1 \end{pmatrix}, \tag{6}$$

where ρ_i is the correlation coefficient that depends on the distance between receiver apertures and the correlation length of irradiance fluctuations. The way to obtain the correlation length as a function of the atmospheric scintillation is defined in [38, Eq. (7)]. Moreover, [38, Eqs. (11) and (15)] presents how to calculate the correlation coefficient for the irradiance fluctuation and the small-scale correlation coefficient of C_Y, respectively.

Thus, the V PDF can be calculated by applying the Moschopoulos theorem according to [29] and [40]. Next, the statistical distribution of the total received irradiance, I, can be directly obtained by averaging the PDF of V (seen as a conditional one) over the PDF of the gamma distribution characterizing the variable X. Since α represents the effective number of small scale turbulent eddies for each of the N receiving channels, it is reasonable to assume $\alpha \in \mathbb{N}$, and after some mathematical manipulations, it is possible to obtain the PDF of the combined received irradiance as

$$f_I(I) = \frac{2}{[\det(A)]^{\alpha}\Gamma(\alpha_x)} \sum_{i=1}^{N'} \sum_{m=1}^{\alpha_i} \frac{c_{mi}}{\Gamma(m)} \lambda_i^{\frac{m-\alpha_x}{2}} \alpha_x^{\frac{m+\alpha_x}{2}} \times I^{N\alpha-1-\frac{m-\alpha_x}{2}} K_{m-\alpha_x}\left(2\sqrt{\frac{\alpha_x I}{\lambda_i}}\right). \tag{7}$$

where $\{\lambda_i\}_{i=1}^{N}$ are the eigenvalues of the matrix $A = DC$, with D being a $N \times N$ diagonal matrix with entries β for $i = 1 \ldots N$, $C = \sqrt{C_Y}$ is a $N \times N$ positive definite correlation matrix, and $\det(A) = \prod_{i=1}^{N} \lambda_i$. Moreover, N' denotes the number of different eigenvalues of matrix A and $\Gamma(\cdot)$ denotes the Gamma function, and $K_v(\cdot)$ is the modified Bessel function of the second kind and order v. Finally, c_{mi} is a coefficient depending on I and arising from the partial fraction expansion procedure written as

$$c_{mi} = \frac{1}{(\alpha_i - m)!} \frac{\mathrm{d}^{\alpha_i - m}}{\mathrm{d}w^{\alpha_i - m}} \left[\prod_{\substack{j=1 \\ j \neq i}}^{N'} \frac{1}{(w - d_j)^{\alpha_j}} \right]_{w=d_i} = \frac{1}{(\alpha_i - m)!} \sum_{k_1 + \ldots \hat{i} \ldots + k_{N'} = \alpha_i - m} \binom{\alpha_i - m}{k_1 \ldots \hat{i} \ldots k_{N'}} \times \prod_{\substack{j=1 \\ j \neq i}}^{N'} \left[(-1)^{k_j} (\alpha_j)_{k_j} (d_i - d_j)^{-\alpha_j - k_j} \right], \tag{8}$$

where $\hat{i}$ means that k_i is omitted. The term $(\alpha_j)_{k_j}$ represents the Pochhammer symbol with $d_i = -I/\lambda_i$, α_i is the product of the algebraic multiplicity of the eigenvalue, denoted as $\mu_A(\lambda_i)$. Finally, the set of k_i coefficients arises from the multinomial theorem given by

$$\frac{\mathrm{d}^n}{\mathrm{d}x^n}\left(\prod_{j=1}^{N} u_j\right) = (u_1 + \cdots + u_N)^{(n)} = \\ = \sum_{k_1+\underset{\hat{i}}{\ldots}+k_{N'}=n} \binom{n}{k_1, \ldots k_N} \prod_{j=1}^{N} u_j^{(k_j)}, \tag{9}$$

and they are employed after calculating the generalized Leibniz rule, where the latter is required to obtain the c_{mi} coefficients. Finally, it is straightforward to obtain $u_j = (w - d_j)^{-\alpha_j}$.

Two particular scenarios can be considered from (7), i.e., first when the scintillation sequences are completely uncorrelated; and second when they are totally correlated. For the first scenario, channels are considered completely independent and the correlation matrix, C_Y, is reduced to a diagonal matrix. For this case, $X \sim \mathcal{G}(\alpha_x, \beta_x)$ and $V = \sum_{i=1}^{N} Y_i \sim \mathcal{G}(N\alpha, 1/(N\alpha))$, with $\sim \mathcal{G}(\cdot)$ denoting a gamma variate. Then the PDF of the received normalized irradiance can be obtained as [29]

$$f_I(I) = \frac{2(\alpha_x N\alpha)^{\frac{N\alpha+\alpha_x}{2}}}{\Gamma(N\alpha)\Gamma(\alpha_x)} I^{\frac{N\alpha+\alpha_x}{2}-1} K_{N\alpha-\alpha_x}\left(2\sqrt{\alpha_x N\alpha I}\right). \tag{10}$$

The second scenario consists of receiving N totally correlated small-scale irradiance fluctuations. Hence, $V = \sum_{i=1}^{N} Y_i \sim \mathcal{G}(\alpha, 1/(\alpha))$. Then, the irradiance random variable follows a classic GG distribution [35] written as

$$f_I(I) = \frac{2(\alpha_x\alpha)^{\frac{\alpha+\alpha_x}{2}}}{\Gamma(\alpha)\Gamma(\alpha_x)} I^{\frac{\alpha+\alpha_x}{2}-1} K_{\alpha-\alpha_x}\left(2\sqrt{\alpha_x\alpha I}\right); \tag{11}$$

where α_x and α are the large and small scale parameters. In the next sections, we derive new analytical-closed form expressions for evaluating the performance of the flexible OCDMA-FSO network. We consider two user classes affected by MAI, atmospheric turbulence, and different correlation among channels to evaluating the network performance.

IV. ERROR PROBABILITY OF THE FLEXIBLE OCDMA-FSO NETWORK

The error probability is one of the most useful figures of merit to assess a network performance. In this section, we derive the BER expression of the OCDMA network integrated with the FSO link. We use an OOK intensity-modulated system in which each user transmits its assigned code sequence for data bit "1" whereas no signal is sent for data bit "0". Moreover, the transmitted signal is subjected to scintillation due to atmospheric turbulence, hence the irradiance power, I, is considered a random variable with $P_b(e)$ denoting the ABER. Assuming a Gaussian distribution for the MAI [14], then the error probability of the OCDMA fiber channel is averaged over the GG PDF shown in (7) in its generic form (or in (10) and (11) for the two particular scenarios) as: $P_b(e) = \int_0^\infty P_b(e|I) f_I(I)\mathrm{d}I$, with $P_b(e|I) = Q(\sqrt{\gamma_s})$ denoting the error probability conditioning on the irradiance, γ_s represents the SNIR of the OCDMA channel for each user class-$s \in \{1, 2, \ldots, S\}$. The Q−function can be expressed in terms of the complementary error function, erfc(·). Accordingly, both erfc(·) and modified Bessel function used in the GG PDFs presented in (7), (10), and (11) can be rewritten as Meijer G functions using [41, Eqs. (07.34.03.0619.01) and (07.34.03.0605.01)]. Such expressions are therefore rewritten as

$$G_{1,2}^{2,0}\left(z\middle| \begin{matrix} aa-1, a-1/2 \\ \end{matrix}\right) = \sqrt{\pi} z^{a-1}\mathrm{erfc}(\sqrt{z}); \tag{12}$$

$$G_{0,2}^{2,0}\left(z\middle| \begin{matrix} a, b \\ \end{matrix}\right) = 2z^{\frac{a+b}{2}} K_{a-b}\left(2\sqrt{z}\right), \tag{13}$$

where $G_{p,q}^{m,n}[\cdot]$ is the univariate Meijer's G-function [41, Eq. (07.34.02.0001.01)]. Thus, depending on the degree of correlation between sequences, ρ, it is possible to distinguish up to three distinct scenarios, namely, totally correlated, partially correlated, and non-correlated channels. The first scenario with N totally correlated small-scale scintillations represents the limiting case for having a single-aperture receiver. In contrast, the totally uncorrelated scenario is the second limiting case, in which the maximum benefit from the spatial diversity technique can be obtained. Thus, the expressions for the ABER in these three scenarios can be derived using [41, Eqs. (07.34.21.0013.01)], respectively, as

$$P_b^{tc}(e) = \frac{2^{\alpha+\alpha_x-1}}{4\pi^{3/2}\Gamma(\alpha)\Gamma(\alpha_x)} \\ \times G_{5,2}^{2,4}\left(\frac{8\gamma_0}{(\alpha_x\alpha)^2}\middle| \begin{matrix} \frac{1-\alpha}{2}, \frac{2-\alpha}{2}, \frac{1-\alpha_x}{2}, \frac{2-\alpha_x}{2}, 1 \\ 0, \frac{1}{2} \end{matrix}\right) \tag{14}$$

$$P_b^{nc}(e) = \frac{2^{N\alpha+\alpha_x-1}}{4\pi^{3/2}\Gamma(N\alpha)\Gamma(\alpha_x)} \\ \times G_{5,2}^{2,4}\left(\frac{8\gamma_0}{(\alpha_x N\alpha)^2}\middle| \begin{matrix} \frac{1-N\alpha}{2}, \frac{2-N\alpha}{2}, \frac{1-\alpha_x}{2}, \frac{2-\alpha_x}{2}, 1 \\ 0, \frac{1}{2} \end{matrix}\right) \tag{15}$$

$$P_b^{pc}(e) = \frac{1}{4\pi^{3/2}[\det(A)]^{\alpha}\Gamma(\alpha_x)} \sum_{i=1}^{N'} \sum_{m=1}^{\alpha_i} \frac{\lambda_i^{\frac{m-\alpha_x}{2}} \alpha_x^{\frac{m+\alpha_x}{2}}}{\Gamma(m)(\alpha_i - m)!} \\ \times \sum_{k_1+\underset{\hat{i}}{\ldots}+k_{N'}=\alpha_i-m} \binom{\alpha_i - m}{k_1 \ldots k_{N'}} 2^{2N\alpha-m+\alpha_x} \\ \times 2^{\sum_{\substack{j=1 \\ j\neq i}}^{N'}[-2\alpha_j-2k_j]} \\ \times \prod_{\substack{j=1 \\ j\neq i}}^{N'} \left[(-1)^{k_j}(\alpha_j)_{k_j}\left(\frac{-1}{\lambda_i} + \frac{1}{\lambda_j}\right)^{-\alpha_j-k_j}\right] \\ \times \left(\frac{\alpha_x}{\lambda_i}\right)^{-(N\alpha-\frac{m-\alpha_x}{2}+\sum_{\substack{j=i \\ j\neq i}}^{N'}[-\alpha_j-k_j])} \\ \times G_{5,2}^{2,4}\left(\frac{8\gamma_0\lambda_i^2}{\alpha_x^2}\middle| \begin{matrix} A, B, C, D, 1 \\ 0, \frac{1}{2} \end{matrix}\right); \tag{16}$$

where the SNIR, γ_0, is given in (5) and

$$A = \frac{1+\sum_{\substack{j=1 \\ j\neq i}}^{N'}[\alpha_j+k_j]-N\alpha}{2}, \quad C = \frac{1+\sum_{\substack{j=1 \\ j\neq i}}^{N'}[\alpha_j+k_j]-N\alpha+m-\alpha_x}{2},$$

$$B = \frac{2+\sum_{\substack{j=1 \\ j\neq i}}^{N'}[\alpha_j+k_j]-N\alpha}{2}, \quad D = \frac{2+\sum_{\substack{j=1 \\ j\neq i}}^{N'}[\alpha_j+k_j]-N\alpha+m-\alpha_x}{2}.$$

In addition, recall that α_x describes the effective number of large-scale turbulent cells, and α is the effective number of small-scale eddies. These parameters are defined in [32, Chapter 12 Eq. (68)], both dependent on Rytov variance written as $\sigma_R^2 = 1.23\, C_n^2 k^{7/6} L^{11/6}$, where C_n^2 is the refraction index structure, which is directly related to the turbulence strength; k is the wave number and L represents the propagation path length. Thus, the variance of these parameters in the different simulations determines the existing turbulence.

Figures 2 and 3 show the ABER performance for class−1 and class−2 users, respectively, as a function of the number of simultaneous class-1 users. It is worth mentioning that the Monte-Carlo simulations are performed for all scenarios investigated in this section, and their obtained numerical results fully agree with the analytical counterpart as shown in Fig. 2 and Fig. 3. In the simulations, it is considered a number of FSO receivers varying from 1 to 4 apertures, where $N = 1$ corresponds to the scenario of totally correlated channels indicated in (15). Furthermore, in order to obtain greater benefit from the spatial diversity technique, the photodetectors have a circular receiving area of 500 cm^2. For this area, the separation distance between the openings of the receivers is large enough even for the case of including 4 photodetectors, thus achieving almost totally independent paths. Noteworthy, the correlation coefficient values between 0 and 0.2 are used for any pair of received small-scale sequences, while the large-scale scintillation component is always a common contribution for all of the N receiver apertures, as described in Section III. In addition, for the performance evaluation, weak, moderate and strong turbulence are considered as $C_n^2 = 4 \times 10^{-15}$ m$^{-2/3}$, $C_n^2 = 10^{-14}$ m$^{-2/3}$ and $C_n^2 = 10^{-13}$ m$^{-2/3}$, respectively, as well as different path lengths with $L = 700$ m, $L = 1800$ m and $L = 2500$ m. Table 1 shows the values of all parameters describing the turbulent channel. The values shown for σ_I^2 are obtained assuming that $\rho = 0$ and $X \sim \mathcal{G}(\alpha_x, \beta_x)$ and $V = \sum_{i=1}^{N} Y_i \sim \mathcal{G}(N\alpha, 1/(N\alpha))$, following the notation of Section III, with $\sim \mathcal{G}(\cdot)$ denoting a gamma variate. In addition, the 2-D MWML-OOC parameters are listed in Table 2, with number of wavelengths fixed to $F = 19$ in all cases. The code set has good correlation properties with values of auto-correlation and cross-relation bounded by one at most.

Next, the ABER performance for both classes is plotted in Fig. 2 and Fig. 3. As can be observed from both figures, the ABER worsens as the number of simultaneous users increases. This occurs due to the increased MAI variance, and consequently, to the SNIR reduction. Nevertheless, when the number of class-1 users, U_1, tends to infinity, the numerical limiting value of all equations (14, 15, 16) tends to be equal to 0.5. Furthermore, Figs. 2 and 3 show how sensitive

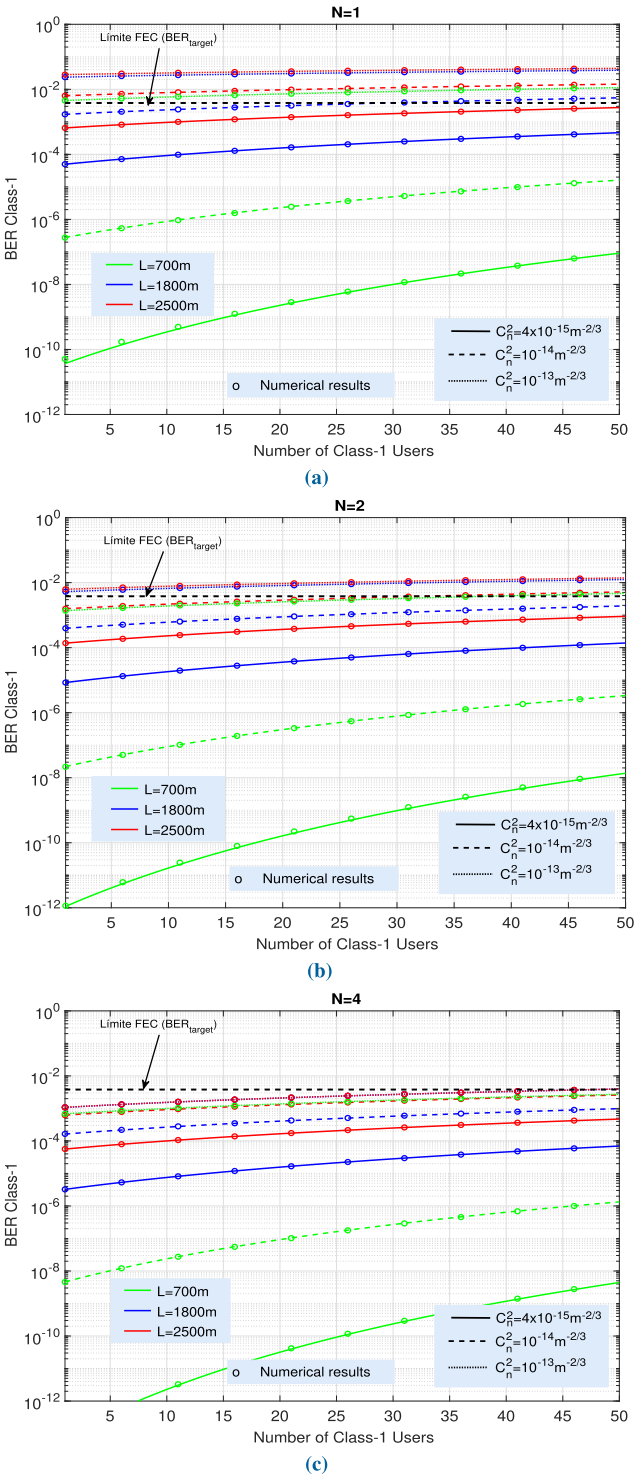

FIGURE 2. Class-1 average BER performance versus the number of simultaneous class-1 users for different turbulence regimes, receiver apertures (N), and spatially correlated scintillations.

the network performance is with respect to an increase in the fading intensity. For weak turbulence values the ABER decreases (solid lines). For $N = 1$ (totally correlated small-scale scintillations), $L = 1800$ and $U_1 = 20$,

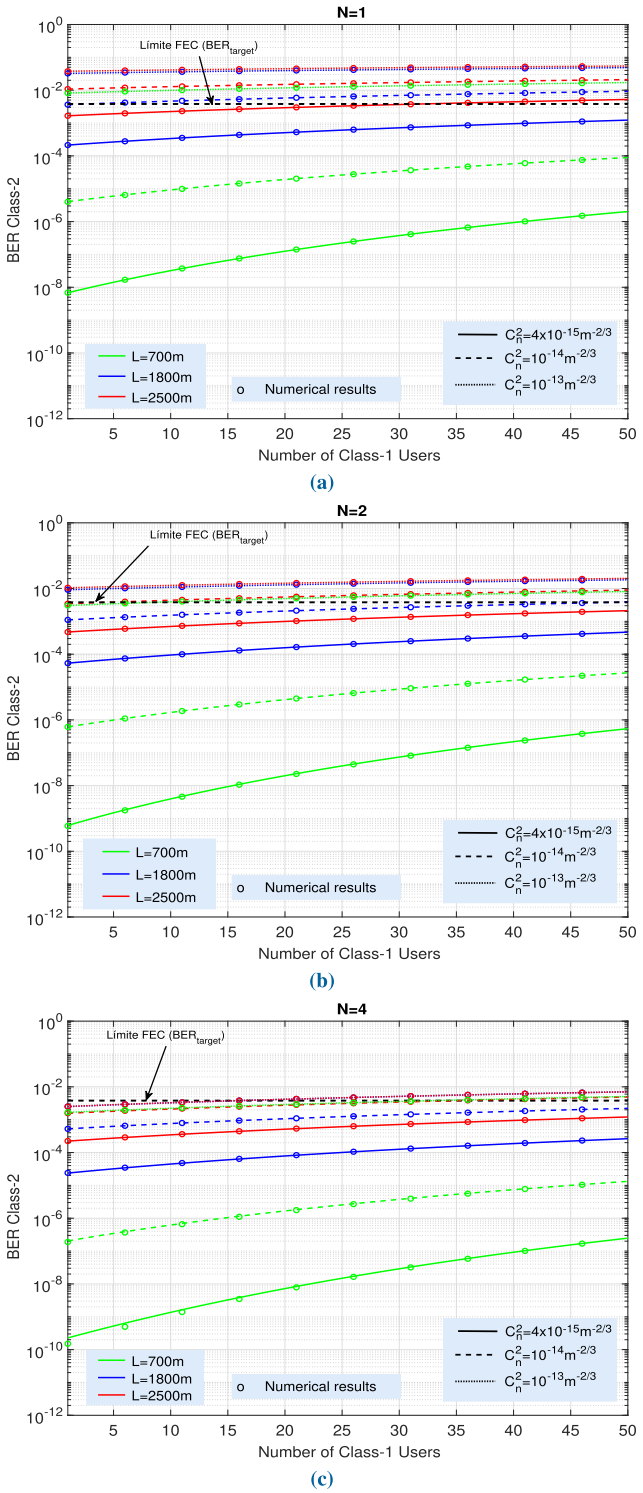

FIGURE 3. Class-2 average BER performance versus the number of simultaneous class-1 users for different turbulence regimes, receiver apertures (N), and spatially correlated scintillations.

we obtain an ABER to 1.6×10^{-4}, for weak turbulence, $C_n^2 = 4 \times 10^{-15}$ m$^{-2/3}$. However, the ABER increases to approximately 3×10^{-2} for strong turbulence (dotted line), $C_n^2 = 10^{-13}$ m$^{-2/3}$.

TABLE 1. Atmospheric channel features. The values for the irradiance variance are obtained assuming $\rho = 0$.

L (m)	C_n^2 ($m^{-2/3}$)	α_x	α	σ_I^2 (N=1)	σ_I^2 (N=2)	σ_I^2 (N=4)
700	4×10^{-15}	50	47	0.0417	0.0309	0.0254
	10^{-14}	21	19	0.1028	0.0752	0.0614
	10^{-13}	4	3	0.6667	0.4583	0.3542
1800	4×10^{-15}	10.2	8.7	0.2243	0.1611	0.1296
	10^{-14}	5.5	3.9	0.4848	0.3333	0.2576
	10^{-13}	4.8	1.2	1.2153	0.7118	0.4601
2500	4×10^{-15}	6.6	5	0.3818	0.2667	0.2091
	10^{-14}	4.3	2.5	0.7256	0.4791	0.3558
	10^{-13}	5.8	1.1	1.2382	0.7053	0.4389

TABLE 2. 2-D MWML-OOC parameters.

Class-1 users			Class-2 users		
Code weight (W_1)	Code length (L_1)	# Users (U_1)	Code weight (W_2)	Code length (L_2)	# Users (U_2)
11	150	50	8	200	20

A similar behavior can be observed for class−2 users from Fig. 3, where the ABER performance is reduced from 3.9×10^{-2} to 5.1×10^{-4}, for $C_n^2 = 10^{-13}$ m$^{-2/3}$ and $C_n^2 = 4 \times 10^{-15}$ m$^{-2/3}$, respectively. The general performance of class−2 (Fig. 3) is more penalized when compared to class−1 (Fig. 2) since the former has low−QoS. For instance, class−1 supports up to 28 users under the forward error correction (FEC) technique limit (see horizontal line in Fig. 2 indicating an ABER $\leq 3.8 \times 10^{-3}$) for $N = 1$, $L = 1800$ and $C_n^2 = 10^{-14}$ m$^{-2/3}$; however, this number is reduced to $U_1 = 4$ users for the ABER of class−2. Nevertheless, if the turbulence intensity becomes weaker ($C_n^2 = 4 \times 10^{-15}$ m$^{-2/3}$), then it is possible to accommodate all users in the error-free transmission zone when FEC is employed, for both class−1 and class−2. It can be further noted how the length of the FSO link influences the final performance of the OCDMA-FSO network. We can observe that the longer the FSO link length, the worse the ABER. Lastly, it can be concluded that the network achieves the best performance under the ideal case, considering the OCDMA channel only.

V. FIGURES OF MERIT IN OUTAGE CONDITIONS

The outage probability along with the outage capacity and the effective data rate under outage conditions are important performance evaluation metrics. Accordingly, they are good indicators of the performance status of a network and useful for system troubleshooting. Thus, in this section, we derive novel closed-form general expressions for these useful performance metrics. The metrics are addressed considering the same network architecture, parameters, and configuration as in the previous section for the sake of analysis consistency.

A. OUTAGE PROBABILITY

The outage probability, denoted as P_{out}, is defined as the probability that the instantaneous SNIR, given by γ in (5), drops below a specified threshold, denoted as γ_{th}, which represents a limiting value above which the channel quality is satisfactory. For received SNIR values below γ_{th}, the received symbols cannot be successfully decoded with probability 1, and the system declares an outage. For this reason, the outage probability gives important information on how to maintain the instantaneous quality metrics below γ_{th}. Thus, P_{out} can be expressed as $P_{out} = \Pr\{\gamma_s < \gamma_{th}\}$. Now, using (5), we can express the outage probability in terms of the optical irradiance as

$$P_{out} = \Pr\left\{I < \sqrt{\frac{\gamma_{th}}{\gamma_0}}\right\} = \Pr\left\{I < \sqrt{\frac{1}{\gamma_n}}\right\}, \tag{17}$$

where $\gamma_n = \gamma_0/\gamma_{th}$ is the normalized SNIR, and γ_0 is the received SNIR for the user class$-$s in the absence of turbulence. According to the above definition, the outage probability can be derived from the cumulative distribution function (CDF) of the normalized received irradiance under LOS blockage $F_I(I)$ as

$$P_{out} = \int_0^{1/\sqrt{\gamma_n}} f_I(I)\mathrm{d}I = F_I\left[\frac{1}{\sqrt{\gamma_n}}\right]. \tag{18}$$

This CDF function can be calculated substituting (7), (10) or (11) into (18) so that the outage probability can be derived for the cases of partially correlated, uncorrelated or totally correlated scintillations, respectively. The integration is solved in the same manner for the three cases as follows: first, applying the equivalence between the Meijer-G and the Bessel K functions [41, Eq. (03.04.26.0009.01)]; and second, using [41, Eq. (07.34.21.0003.01)] to solve the resulting integral. Hence, the outage probability can be written in a closed-form manner for the three cases (partially, totally and uncorrelated scintillations) respectively, as follows

$$\begin{aligned} P_{out}^{pc} = {} & \frac{1}{[\det(A)]^{\alpha}\Gamma(\alpha_x)} \sum_{i=1}^{N'} \sum_{m=1}^{\alpha_i} \frac{1}{\Gamma(m)} \frac{\lambda_i^{\frac{m-\alpha_x}{2}} \alpha_x^{\frac{m+\alpha_x}{2}}}{(\alpha_i - m)!} \\ & \times \sum_{k_1+\ldots\overset{\hat{i}}{+}k_{N'}=\alpha_i-m} \binom{\alpha_i - m}{k_1 \ldots \overset{\hat{i}}{} k_{N'}} \\ & \times \prod_{\substack{j=1 \\ j\neq i}}^{N'} \left[(-1)^{k_j} (\alpha_j)_{k_j} \left(\frac{-1}{\lambda_i} + \frac{1}{\lambda_j}\right)^{-\alpha_j - k_j} \left(\sqrt{\gamma_n}\right)^{-M} \right. \\ & \left. \times G_{1,3}^{2,1}\left(\frac{\alpha_x}{\lambda_i\sqrt{\gamma_n}} \middle| \begin{matrix} 1-M \\ \frac{m-\alpha_x}{2}, -\frac{m-\alpha_x}{2}, -M \end{matrix}\right)\right], \end{aligned} \tag{19}$$

$$\begin{aligned} P_{out}^{tc} = {} & \frac{(\alpha_x\alpha)^{\frac{\alpha+\alpha_x}{2}}}{\Gamma(\alpha)\Gamma(\alpha_x)} \left(\sqrt{\gamma_n}\right)^{-\frac{\alpha+\alpha_x}{2}} \\ & \times G_{1,3}^{2,1}\left(\frac{\alpha_x\alpha}{\sqrt{\gamma_n}} \middle| \begin{matrix} 1-\frac{\alpha+\alpha_x}{2} \\ \frac{\alpha-\alpha_x}{2}, -\frac{\alpha-\alpha_x}{2}, -\frac{\alpha+\alpha_x}{2} \end{matrix}\right). \end{aligned} \tag{20}$$

$$\begin{aligned} P_{out}^{nc} = {} & \frac{(\alpha_x N\alpha)^{\frac{N\alpha+\alpha_x}{2}}}{\Gamma(N\alpha)\Gamma(\alpha_x)} \left(\sqrt{\gamma_n}\right)^{-\frac{N\alpha+\alpha_x}{2}} \\ & \times G_{1,3}^{2,1}\left(\frac{\alpha_x N\alpha}{\sqrt{\gamma_n}} \middle| \begin{matrix} 1-\frac{N\alpha+\alpha_x}{2} \\ \frac{N\alpha-\alpha_x}{2}, -\frac{N\alpha-\alpha_x}{2}, -\frac{N\alpha+\alpha_x}{2} \end{matrix}\right). \end{aligned} \tag{21}$$

where $M = N\alpha - \frac{m-\alpha_x}{2} - \alpha_j - k_j$. The results obtained via (19)$-$(21) are shown in Figs. 4 and 5 for different values of turbulence conditions, degrees of correlation, and number of FSO receivers. These figures show the outage probability versus the number of class-1 users for class$-$1 and class$-$2. In both figures, we have assumed the performance limiting case as $\gamma_{th} = 0$ dB, i.e., the required quality target must be exactly the electrical SNIR in absence of turbulence. Interestingly, these optical systems must work with an electrical SNIR several dB higher than the established γ_{th} in the absence of turbulence. Again, better results are obtained for a higher number of FSO receivers, shorter FSO link lengths, and weak turbulence. Thus, class$-$1 users show better performance. For example, for weak turbulence ($C_n^2 = 4 \times 10^{-15}$ m$^{-2/3}$), with $N = 4$ receivers and $L = 1800$ m, the outage probability for class$-$1 users is approximately 4×10^{-6} when 40 simultaneous users are active in class$-$1. This outage probability is increased to $P_{out} \approx 10^{-5}$ for class$-$2 users, under the same conditions. When the turbulence intensity becomes strong ($C_n^2 = 10^{-13}$ m$^{-2/3}$), the outage probability is $P_{out} \approx 5.3 \times 10^{-3}$ and 10^{-2} for class$-$1 and class$-$2 users, respectively, which means that the channel quality is guaranteed 99.47% and 99% of the time, respectively.

B. EFFECTIVE DATA RATE IN OUTAGE CONDITIONS

We consider the same network configuration for the coming analysis as the previous section for the sake of consistency. Assuming that the instantaneous channel state information is not known at the transmitter, the system will achieve its maximum data rate, R_b, for the limiting case $\gamma_s = \gamma_{th}$, given by the outage capacity as follows

$$C_{out} = B\log_2(1 + \gamma_{th}), \tag{22}$$

where B is the received signal bandwidth. For a completely generic behavior, we prefer to use the normalized outage capacity given by $\hat{C}_{out} = \log_2(1 + \gamma_{th})$. Hence, for $R_b = \hat{C}_{out}$, we consider that the system is not in outage and the transmitted data is correctly received, which occurs with a probability of $(1 - P_{out})$. The value of γ_{th} is typically a design parameter based on the acceptable outage probability. Hence, the effective data rate in outage, R_{out}, is defined as the average rate correctly received over a large number of transmissions (a transmission burst) [42] as follows:

$$R_{out} = (1 - P_{out})\log_2(1 + \gamma_{th}) \quad \text{[bits/s/Hz]}. \tag{23}$$

Equation (23) is normalized as an average data rate per Hz so that results can be easily adapted to the bandwidth of any network.

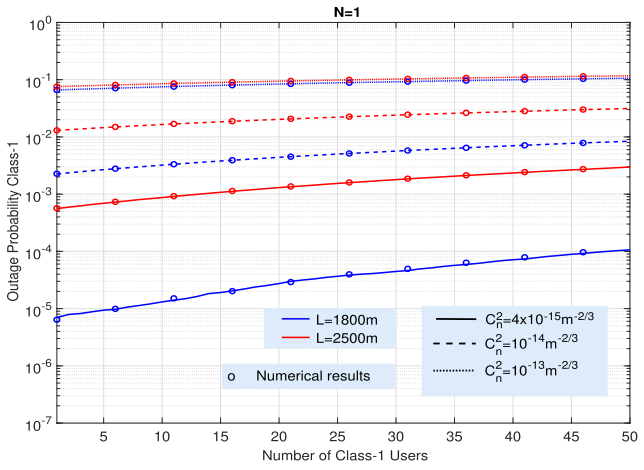

(a)

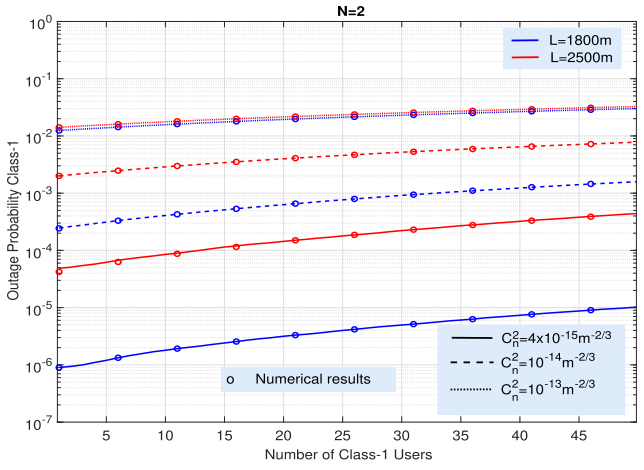

(b)

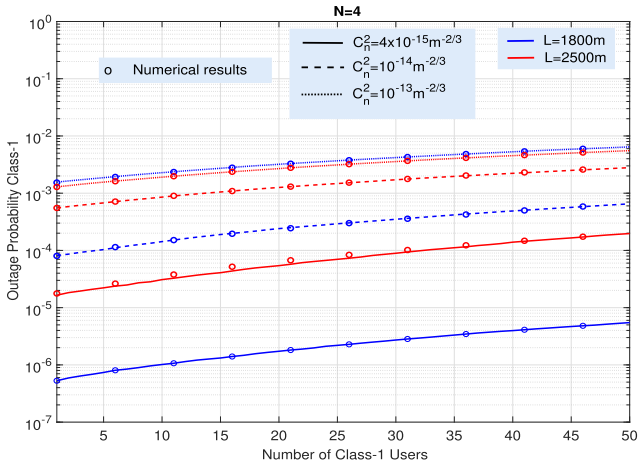

(c)

FIGURE 4. Class-1 outage probability versus the number of simultaneous class-1 users for different turbulence regimes, receiver apertures (N), and spatially correlated scintillations.

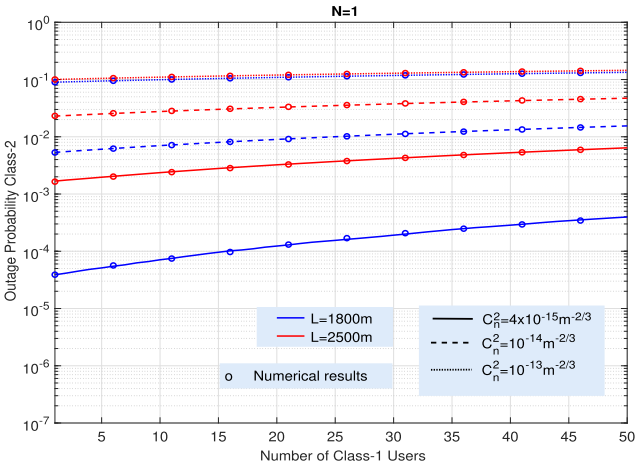

(a)

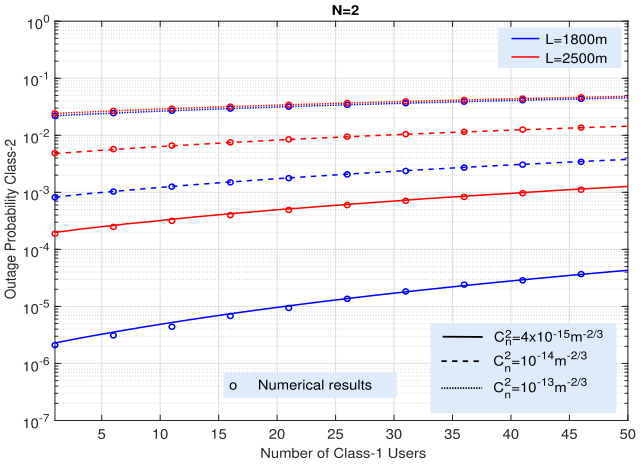

(b)

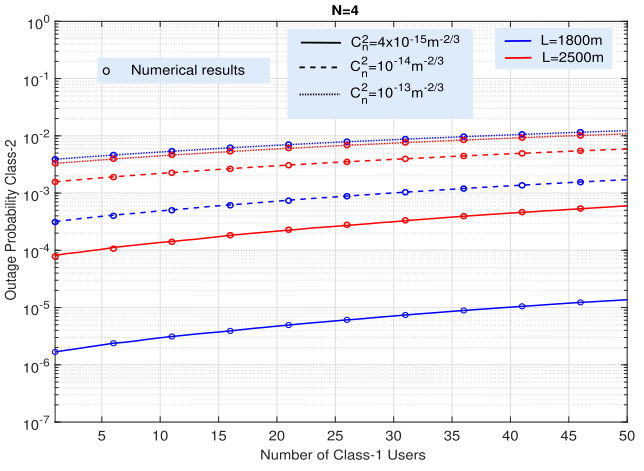

(c)

FIGURE 5. Class-2 outage probability versus the number of simultaneous class-1 users for different turbulence regimes, receiver apertures (N), and spatially correlated scintillations.

Figures 6 and 7 show the effective data rate in outage conditions for class−1 users versus the outage probability for two representative SNIRs in absence of turbulence, $\gamma_0 = 10$ dB and $\gamma_0 = 20$ dB, respectively. For these two cases, we present the behavior associated to different link lengths and three different turbulence conditions: strong

($C_n^2 = 10^{-13}$ m$^{-2/3}$, dotted line), moderate ($C_n^2 = 10^{-14}$ m$^{-2/3}$, dashed line), and weak ($C_n^2 = 4 \times 10^{-15}$ m$^{-2/3}$, solid line) for $N = 1 \ldots 4$ FSO receivers. We show only the performance for class−1 users since class−2 has a similar behavior. Here, the same conditions listed in Table 1 are assumed, maintaining the number of available wavelengths $F = 19$ for all cases. From these figures, one can straightforwardly realize the outage probability (the one that maximizes the effective data rate in outage conditions) decreases with the reduction of the turbulence intensity.

One can note from such Figs. 6 and 7 for $N = 1$ and strong turbulence ($C_n^2 = 10^{-13}$ m$^{-2/3}$), that outage rate has very small values for a small range of outage probability due to the requirement of correctly decoding bits transmitted under severe fading, and increases dramatically as outage probability increases. Note, however, that these high capacity values for large outage probabilities have higher probability of incorrect data reception. After applying the spatial diversity technique and increasing the number of photodetectors considered, the system allows an increase in the transmission rate from an outage probability value equal to zero even for the case of strong scintillation levels. Additionally, if a high quality target is required to achieve a higher channel capacity, then the system is expected to suffer a higher outage probability since $P_{out} = \Pr\{\gamma_s < \gamma_{th}\}$. This leads to poorer effective data rates. Furthermore, if we compare the figures, as expected, the resulting behavior is scaled by the γ_0 parameter.

Finally, Figs. 6 and 7 also show that the average rate correctly received can be maximized by finding the γ_{th} that maximizes R_{out}. For example, for the case of weak turbulence, $L = 1800$ m and $\gamma_0 = 20$ dB, the maximum values of R_{out} are, respectively, 4.222, 4.479 and 4.606 bits/s/Hz for $N = 1, 2$ and 4. These values correspond to an outage probability $P_{out} = 0.151, 0.125$, and 0.112, respectively, and, from (23), to a γ_{th} of 14.83, 15.28 and 15.49 dB, respectively. If we consider strong turbulence represented by the dotted line, and for the same other conditions, we obtain $R_{out} = 2.806$, 3.274, and 3.656 bits/s/Hz corresponding to $P_{out} = 0.417, 0.307$ and 0.241, for $N = 1, 2$ and 4, respectively. Then, the resulting γ_{th} are: 14.33, 14.05 and 14.34 dB. As a consequence, and from Figs. 6 and 7, it is straightforward to check how, when the turbulence intensity is harder, then he maximum average data rate correctly received is obtained when allowing a more severe outage probability (a less temporal availability of the link), as commented above.

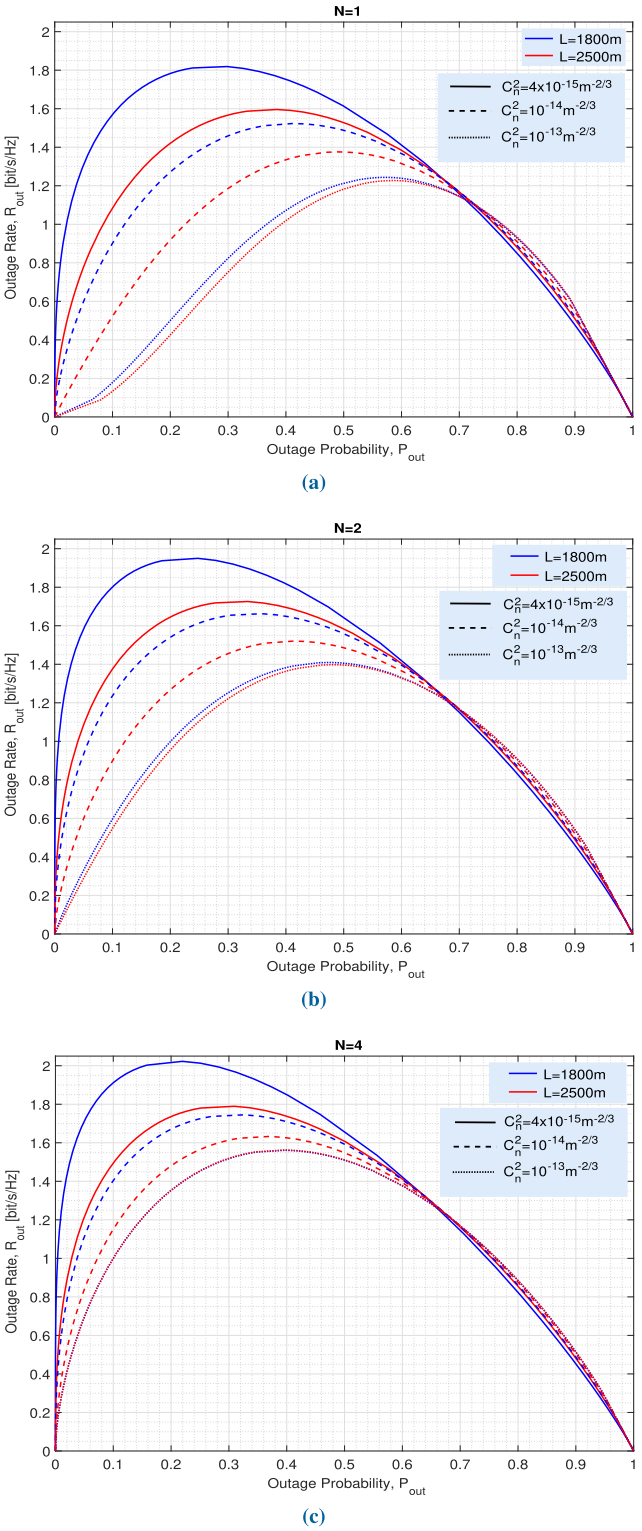

FIGURE 6. Class-1 outage rate versus the outage probability for different turbulence regimes, receiver apertures (N), spatially correlated scintillations and $\gamma_0 = 10dB$.

C. ERGODIC CAPACITY

We develop the ergodic capacity taking into account the same network configuration used in the previous sections. Generally, the outage capacity accounts for transmission schemes that allow errors to occur in a channel, i.e., data lost can happen during deep fades. Nevertheless, there is also a more restrictive capacity definition, the so-called ergodic (Shannon) capacity. The ergodic capacity provides an estimation of the maximum achievable information rate transmitted when the signal is affected by every possible

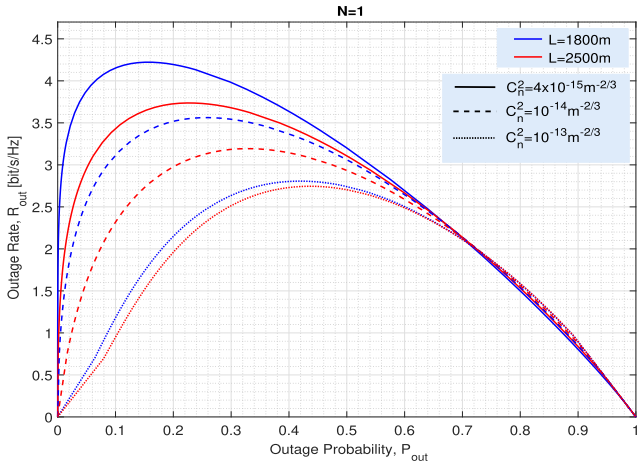

(a)

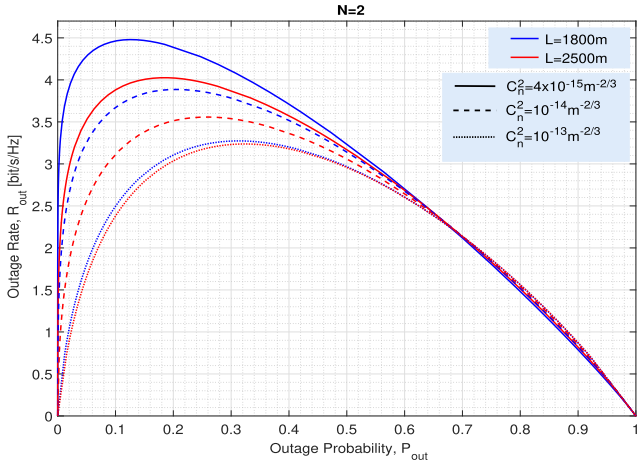

(b)

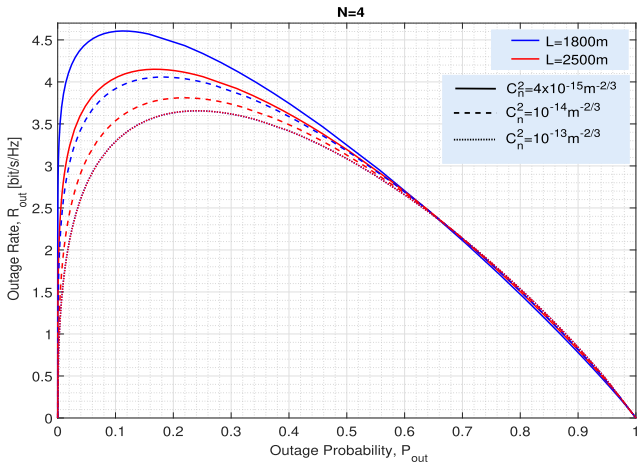

(c)

FIGURE 7. Class-1 outage rate versus the outage probability for different turbulence regimes, receiver apertures (N), spatially correlated scintillations and $\gamma_0 = 20dB$.

channel turbulence effect [42]. It can be calculated by

$$C_{erg} = \int_0^\infty B \log_2 (1 + \gamma_0 I^2) f_I(I) \mathrm{d}I, \tag{24}$$

where B is the received signal bandwidth, $f_I(I)$ is the pdf of the corresponding irradiance distribution model (Eqs. (7), (10), and (11)), with γ_0 defined in (5). In this respect, it is worth mentioning that the ergodic capacity is also referred to as the average of the instantaneous capacity for an AWGN channel. Hence, it should be remarked that for an ergodic capacity, the rate transmitted over the channel is constant. This implies that the transmitter cannot adjust its transmission strategy based on the state of the channel. Consequently, unfavorable channel states may lead to a reduction in ergodic capacity, as the transmission strategy must account for them beforehand.

Then, Equation (24) is solved for the three cases represented by Eqs. (7), (10) and (11), and to do so, we employ the equivalences between the Meijer-G and Bessel K functions [41, Eq. (03.04.26.0009.01)], and either the natural logarithm [41, Eq. (01.04.26.0003.01)]. Next, we apply [41, Eq. (07.34.21.0013.01)] to solve the resulting integral involving the product of two Meijer-G functions. Thus, the ergodic capacity is derived as a closed-form expression for the three cases (partially, totally and uncorrelated scintillations), respectively, as follows:

$$\begin{aligned} C_{erg}^{pc} = {} & \frac{B}{4\pi \ln 2} \frac{1}{[\det(A)]^{\alpha} \Gamma(\alpha_x)} \sum_{i=1}^{N'} \sum_{m=1}^{\alpha_i} \frac{\lambda_i^{\frac{m-\alpha_x}{2}} \alpha_x^{\frac{m+\alpha_x}{2}}}{\Gamma(m)(\alpha_i - m)!} \\ & \times \sum_{k_1 + \ldots \overset{\hat{i}}{+} k_{N'} = \alpha_i - m} \binom{\alpha_i - m}{k_1 \ldots \overset{\hat{i}}{k_{N'}}} \\ & \times 2^{2N\alpha - m + \alpha_x + \sum_{\substack{j=1 \\ j \neq i}}^{N'} [-2\alpha_j - 2k_j]} \\ & \times \prod_{\substack{j=1 \\ j \neq i}}^{N'} \left[(-1)^{k_j} (\alpha_j)_{k_j} \left(\frac{-1}{\lambda_i} + \frac{1}{\lambda_j} \right)^{-\alpha_j - k_j} \right] \\ & \times \left(\frac{\alpha_x}{\lambda_i} \right)^{-(N\alpha - \frac{m-\alpha_x}{2} + \sum_{\substack{j=i \\ j \neq i}}^{N'} [-\alpha_j - k_j])} \\ & \times G_{6,2}^{1,6} \left(\frac{16\lambda_i^2}{\alpha_x^2} \gamma_0 \middle| \begin{matrix} 1, 1, A, B, C, D \\ 1, 0 \end{matrix} \right), \end{aligned} \tag{25}$$

$$\begin{aligned} C_{erg}^{tc} = {} & \frac{B}{4\pi \ln 2} \frac{2^{\alpha + \alpha_x}}{\Gamma(\alpha)\Gamma(\alpha_x)} \\ & \times G_{6,2}^{1,6} \left(\frac{16\gamma_0}{(\alpha_x \alpha)^2} \middle| \begin{matrix} 1, 1, \frac{1-\alpha}{2}, \frac{2-\alpha}{2}, \frac{1-\alpha_x}{2}, \frac{2-\alpha_x}{2} \\ 1, 0 \end{matrix} \right), \end{aligned} \tag{26}$$

$$\begin{aligned} C_{erg}^{nc} = {} & \frac{B}{4\pi \ln 2} \frac{2^{N\alpha + \alpha_x}}{\Gamma(N\alpha)\Gamma(\alpha_x)} \\ & \times G_{6,2}^{1,6} \left(\frac{16\gamma_0}{(\alpha_x N\alpha)^2} \middle| \begin{matrix} 1, 1, \frac{1-N\alpha}{2}, \frac{2-N\alpha}{2}, \frac{1-\alpha_x}{2}, \frac{2-\alpha_x}{2} \\ 1, 0 \end{matrix} \right); \end{aligned} \tag{27}$$

where γ_0 is given in Eq. (2) and

$$A = \frac{1+\sum_{\substack{j=1\\ j\neq i}}^{N'}[\alpha_j+k_j]-N\alpha}{2}, \quad C = \frac{1+\sum_{\substack{j=1\\ j\neq i}}^{N'}[\alpha_j+k_j]-N\alpha+m-\alpha_x}{2},$$

$$B = \frac{2+\sum_{\substack{j=1\\ j\neq i}}^{N'}[\alpha_j+k_j]-N\alpha}{2}, \quad D = \frac{2+\sum_{\substack{j=1\\ j\neq i}}^{N'}[\alpha_j+k_j]-N\alpha+m-\alpha_x}{2}.$$

Subsequently, we plot the normalized ergodic capacity as a function of the number of simultaneous class−1 users in Figs. 8 and 9 for class−1 and class−2, respectively, considering different turbulence conditions (strong, moderate, and weak), and up to four FSO receivers. For the sake of clarity and conciseness, the same network configuration as previously considered is used here for the analysis of the ergodic capacity. The weaker the turbulence intensity, the closer the performance gets to the ideal OCDMA channel. In addition, notice that the spatial diversity technique exhibits its best performance for $N = 4$. This is due to the proposed receiving area, 500 cm^2, a value for which the degree of correlation among small-scale scintillation sequences is not very remarkable, i.e., optical receptors can be sufficiently separated. For example, considering weak turbulence (solid lines) and $L = 2500$ m (red line) for $N = 1$ in class−1 users, the capacity reaches around 6.01 bits/s/Hz under 30 simultaneous users, and increases up to approximately 6.2 bits/s/Hz for N = 4. Finally, a higher capacity value is associated to users belonging to class−1, i.e., to those with higher QoS. Thus, the ergodic capacity shows the transmission rate limit in fading channels for each turbulence regime. However, under typical turbulence conditions, the atmospheric channel is considered as a slow fading channel related to the transmission rate.

VI. FINAL DISCUSSION

With the aim of providing a comprehensive analysis of all the obtained results and with the explicit objective of elucidating the entirety of the work carried out in this manuscript, we now present a final discussion encompassing all that has been outlined in Sections IV and V.

We started our analysis by deriving and analyzing the impact of the error probability in the proposed network to assess its performance Thus, and as shown in Figs. 2 and 3, under strong turbulence, the network achieves unaccepted ABER levels, even above the FEC limit. Nevertheless, the system can accommodate all users under the error-free transmission regime when FEC is employed, if the number of class-1 users, U_1, is less than 28 or 4 (class−1 and class−2, respectively), $L = 1800$ m, under moderate turbulence and with $N = 1$ receiver aperture. In contrast, all users of class−1 and class−2 (50 and 20, respectively, see Table 2) can technically achieve error-free transmissions for $N = 4$ under the same scenario.

However, the ABER may not provide enough information when the system is operating under fading channels, and other different figures of merit should be considered in outage conditions. In particular, any transmission in our proposed scenario may be affected by turbulence-induced fading where the received irradiance of an optical wave can be modeled as a modulation process in which small-scale fluctuations are multiplicatively modulated by statistically independent large-scale fluctuations, as explained in Section III. For that reason,

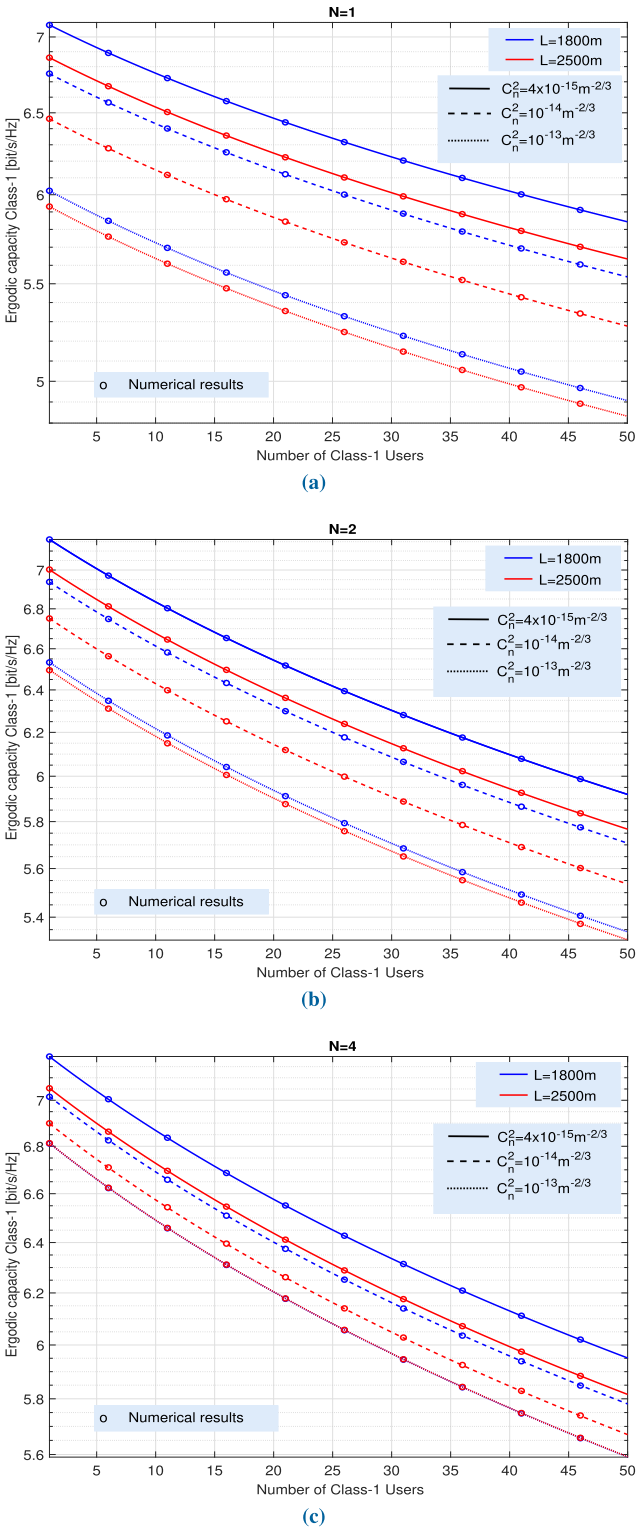

FIGURE 8. Class-1 ergodic capacity versus the number of simultaneous class-1 users for different turbulence regimes.

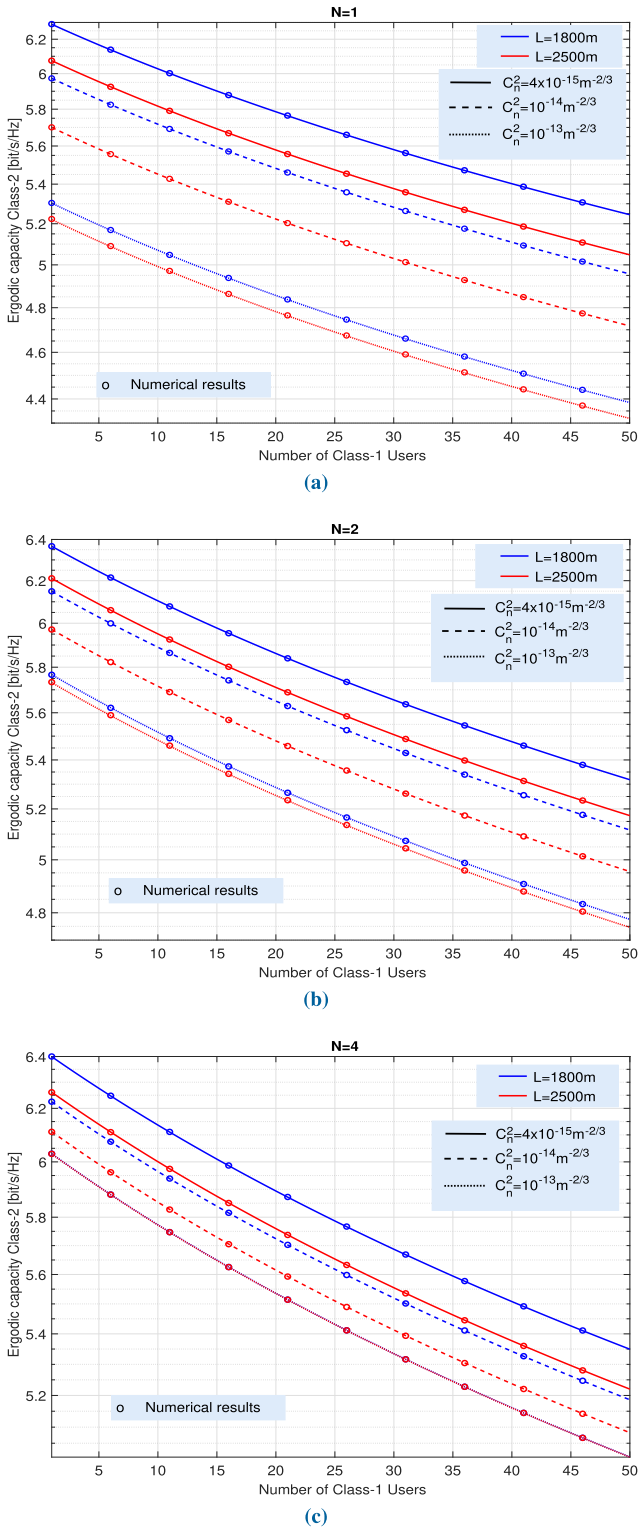

FIGURE 9. Class-2 ergodic capacity versus the number of simultaneous class-1 users for different turbulence regimes.

the outage probability and ABER are usually combined with both slow fading component and fast fading part. In this respect, and from Figs. 4 and 5, the results shown in Section V are promising, since for a moderate turbulence ($C_n^2 = 10^{-14}$ $m^{-2/3}$) represented by dashed lines, the outage probability is as low as $P_{out} \approx 2.9 \times 10^{-4}$ and $P_{out} \approx 8.6 \times 10^{-4}$ for class−1 and class−2 users, respectively, for 25 simultaneous class−1 users, and $N = 4$ FSO receivers with $L = 1800$ m. These values ensure that the target performance will be guaranteed 99.97% and 99.91% of the time, for class−1 and for class−2 users, respectively, whereas for $N = 2$, the outage probabilities increase to $P_{out} = 7.6 \times 10^{-4}$ and 2×10^{-3}.

In terms of capacity limits, we have assumed that the information about the statistical distribution of the fading is known at the receiver side. Hence, we first analyzed the effective data rate in outage conditions. In this way, the effective data rate, regarding any fading state, must be lower than the one defined by the outage capacity, given by (22). This capacity is only maintained when the system is not in outage. For example, the results in Figs. 6 and 7 show that the effective data rate in outage conditions can be maximized by correctly choosing the quality target, γ_{th}, that provides a different value depending on the turbulence conditions. Acceptable outage rate occurs if the outage probability is intentionally high, and when very strong turbulence conditions are affecting the system, as shown in Fig. 6 (see dotted lines). Nevertheless, the allowed outage probability decreases significantly when the turbulence intensity is reduced. Accordingly, for weak turbulence (solid lines), $N = 2$, and $L = 2500$ m, represented by the red line, the maximum R_{out} is 1.73 bits/s/Hz for $P_{out} \approx 0.3$, i.e., the target performance is guaranteed 70% of the time, maintaining a normalized outage rate around 1.73 bit/s/Hz. In contrast, under the same condition (weak turbulence, $N = 2$, $L = 2500$ and 25 users), the network achieves $C_{erg} \approx 6.26$ and 5.6 bits/s/Hz for class−1 and class−2 users, respectively, as shown in Figures 8 and 9. Therefore, for a network with 2 FSO receivers affected by a turbulence regime given by $C_n^2 = 4 \times 10^{-15}$ $m^{-2/3}$, and $\alpha_x = 10.5$, $\alpha = 3$, if the scintillations are completely uncorrelated, the transmitter could be separated from the receiver by a distance of up to 4.2 km with error-free transmissions. This can be achieved with $P_{out} = 2.9 \times 10^{-4}$ and 4.7×10^{-4} for class-1 and class-2 users, respectively, and considering up to 50 class-1 simultaneous users, which renders an availability of 99.97% of the time.

VII. CONCLUDING REMARKS

In this work, we have extensively analyzed the performance of a flexible hybrid OCDMA-FSO network under gamma-gamma turbulence-induced fading. The proposed network allows users to transmit in a fully asynchronous manner and their signal bandwidth is used according to their required transmission rate. The users' transmitted signal is collected by multiple FSO receivers using an EGC spatial diversity technique. We have derived new analytical closed-form expressions to evaluate the network performance in terms of ABER, outage probability, effective data rate under outage conditions and ergodic capacity. The degree of correlation among FSO receivers is one of the main performance limiting

factors of the network, so we have considered a range large enough to show the positive impact of the spatial diversity technique on performance. However, the network is also severely affected by the intensity of turbulence. Interested readers are referred to [38] for further details on the effect of atmospheric correlation on FSO systems.

Research into hybrid OCDMA-FSO networks is currently experiencing a phase of growth, presenting numerous prospects for future exploration. Several techniques can be explored to improve spectral efficiency, a key factor in the deployment of OCDMA-FSO networks, enabling a larger user pool and higher data rates. One such approach is adaptive modulation, which allows the signal modulation to be adjusted in response to communication channel conditions. Alternatively, the application of machine learning techniques for diverse network functions such as resource planning, signal recovery, digital coding, equalization, and interference mitigation, presents another avenue for research. In addition, a future implementation could involve the incorporation of spatial diversity into the FSO transmitter, creating a multiple-input multiple-output system. Such an enhancement would potentially improve channel capacity, spectral efficiency, and signal quality.

DISCLOSURES

The authors declare no conflicts of interest.

REFERENCES

[1] F. J. Effenberger and D. Zhang, "WDM-PON for 5G wireless fronthaul," *IEEE Wireless Commun.*, vol. 29, no. 2, pp. 94–99, Apr. 2022.

[2] Y. Luo, M. Jiang, D. Zhang, and F. Effenberger, "Field trial of network slicing in 5G and PON-enabled industrial networks," *IEEE Wireless Commun.*, vol. 30, no. 1, pp. 78–85, Feb. 2023.

[3] T. R. Raddo, A. L. Sanches, I. Tafur Monroy, and B. V. Borges, "Throughput performance evaluation of multiservice multirate OCDMA in flexible networks," *IEEE Photon. J.*, vol. 8, no. 1, pp. 1–15, Feb. 2016.

[4] D. Neves, A. Sanches, R. Nobrega, H. Mrabet, I. Dayoub, K. Ohno, S. Haxha, I. Glesk, A. Jurado-Navas, and T. Raddo, "Beyond 5G fronthaul based on FSO using spread spectrum codes and graphene modulators," *Sensors*, vol. 23, no. 8, p. 3791, Apr. 2023. [Online]. Available: https://www.mdpi.com/1424-8220/23/8/3791

[5] L. Galdino, T. R. Raddo, A. L. Sanches, L. H. Bonani, and E. Moschim, "Performance comparison of hybrid 1-D WDM/OCDMA and 2-D OCDMA towards future access network migration scenario," in *Proc. 14th Int. Conf. Transparent Opt. Netw. (ICTON)*, Jul. 2012, pp. 1–4.

[6] S. S. Jaffer, A. Hussain, P. V. Klaine, M. Z. Shakir, and M. A. Qureshi, "Hybrid passive optical network–free-space optic-based fronthaul architecture for ultradense small cell network," *Opt. Eng.*, vol. 59, no. 7, Jul. 2020, Art. no. 075104, doi: 10.1117/1.oe.59.7.075104.

[7] E. Ciaramella, Y. Arimoto, G. Contestabile, M. Presi, A. D'Errico, V. Guarino, and M. Matsumoto, "1.28-Tb/s (32 × 40 Gb/s) free-space optical WDM transmission system," *IEEE Photon. Technol. Lett.*, vol. 21, no. 16, pp. 1121–1123, Aug. 2009.

[8] A. Jurado-Navas, A. Tatarczak, X. Lu, J. J. V. Olmos, J. M. Garrido-Balsells, and I. T. Monroy, "850-nm hybrid fiber/free-space optical communications using orbital angular momentum modes," *Opt. Exp.*, vol. 23, no. 26, p. 33721, Dec. 2015. [Online]. Available: https://opg.optica.org/oe/abstract.cfm?URI=oe-23-26-33721

[9] J. Wang, J.-Y. Yang, I. M. Fazal, N. Ahmed, Y. Yan, H. Huang, Y. Ren, Y. Yue, S. Dolinar, M. Tur, and A. E. Willner, "Terabit free-space data transmission employing orbital angular momentum multiplexing," *Nature Photon.*, vol. 6, no. 7, pp. 488–496, Jun. 2012.

[10] L. Yu, X. Sun, S. Shao, Y. Chen, and R. Albelaihi, "Backhaul-aware drone base station placement and resource management for FSO-based drone-assisted mobile networks," *IEEE Trans. Netw. Sci. Eng.*, vol. 10, no. 3, pp. 1659–1668, May 2023.

[11] C. Álvarez-Roa, M. Álvarez-Roa, F. J. Martín-Vega, M. Castillo-Vázquez, T. Raddo, and A. Jurado-Navas, "Performance analysis of a vertical FSO link with energy harvesting strategy," *Sensors*, vol. 22, no. 15, p. 5684, Jul. 2022.

[12] T. Raddo, S. Rommel, and B. Cimoli, "Transition technologies towards 6G networks," *J. Wireless Commun. Netw.*, vol. 100, pp. 1–22, Apr. 2021.

[13] R. Nobrega, T. R. Raddo, A. Jurado-Navas, M. Loiola, A. L. Sanches, and M. Debbah, "A channel loss model for THz networks from 100–600 GHz considering both molecular and water vapor continuum absorptions," *IEEE Open J. Veh. Technol.*, vol. 4, pp. 475–489, 2023.

[14] A. Jurado-Navas, T. R. Raddo, J. M. Garrido-Balsells, B.-H.-V. Borges, J. J. V. Olmos, and I. T. Monroy, "Hybrid optical CDMA-FSO communications network under spatially correlated gamma-gamma scintillation," *Opt. Exp.*, vol. 24, no. 15, p. 16799, Jul. 2016. [Online]. Available: https://opg.optica.org/oe/abstract.cfm?URI=oe-24-15-16799

[15] A. Yadav, S. Kar, and V. K. Jain, "Performance of 1-D and 2-D OCDMA systems in presence of atmospheric turbulence and various weather conditions," *IET Commun.*, vol. 11, no. 9, pp. 1416–1422, Jun. 2017. [Online]. Available: https://digital-library.theiet.org/content/journals/10.1049/iet-com.2016.1008

[16] K. Sasaki, N. Minato, T. Ushikubo, and Y. Arimoto, "First OCDMA experimental demonstration over free space and optical fiber link," in *Proc. OFC/NFOEC Conf. Opt. Fiber Commun./Nat. Fiber Optic Eng. Conf.*, San Diego, CA, USA, Feb. 2008, pp. 1–3.

[17] S. Chaudhary, A. Sharma, X. Tang, X. Wei, and P. Sood, "A cost effective 100 Gbps FSO system under the impact of fog by incorporating OCDMA-PDM scheme," *Wireless Pers. Commun.*, vol. 116, no. 3, pp. 2159–2168, Feb. 2021.

[18] S. Abd El Mottaleb, A. Métwalli, M. Singh, M. Hassib, and M. Aly, "Machine learning FSO-SAC-OCDMA code recognition under different weather conditions," *Opt. Quantum Electron.*, vol. 54, p. 851, Oct. 2022.

[19] M. Rahmani, G. N. Sabri, A. Cherifi, A. S. Karar, and H. Mrabet, "Massive capacity of novel three-dimensional OCDMA-FSO system for next generation of high-data wireless networks," *Trans. Emerg. Telecommun. Technol.*, p. e4871, 2023. https://onlinelibrary.wiley.com/doi/abs/10.1002/ett.4871

[20] S. A. Abd El-Mottaleb, A. Métwalli, T. A. ElDallal, M. Hassib, H. A. Fayed, and M. H. Aly, "Performance evaluation of PDM/SAC-OCDMA-FSO communication system using DPS code under fog, dust and rain," *Opt. Quantum Electron.*, vol. 54, no. 11, p. 750, Nov. 2022.

[21] M. Singh, A. Atieh, M. H. Aly, and S. A. A. El-Mottaleb, "120 Gbps SAC-OCDMA-OAM-based FSO transmission system: Performance evaluation under different weather conditions," *Alexandria Eng. J.*, vol. 61, no. 12, pp. 10407–10418, Dec. 2022. [Online]. Available: https://www.sciencedirect.com/science/article/pii/S1110016822002459

[22] S. Zou, M. M. Karbassian, and H. Ghafouri-Shiraz, "Extended 2D codes supporting multirate and QoS in optical CDMA networks with Poisson and binomial MAI models," *J. Opt. Commun. Netw.*, vol. 5, no. 5, pp. 524–531, May 2013.

[23] I. Glesk, P. R. Prucnal, and I. Andonovic, "Incoherent ultrafast OCDMA receiver design with 2 PS all-optical time gate to suppress multiple-access interference," *IEEE J. Sel. Topics Quantum Electron.*, vol. 14, no. 3, pp. 861–867, Sep. 2008.

[24] J. V. dos Reis Jr., T. R. Raddo, A. L. Sanches, and B. V. Borges, "Fuzzy logic control for the mitigation of environmental temperature variations in OCDMA networks," *J. Opt. Commun. Netw.*, vol. 7, no. 5, pp. 480–488, May 2015.

[25] F. Xu, M.-A. Khalighi, and S. Bourennane, "Impact of different noise sources on the performance of PIN- and APD-based FSO receivers," in *Proc. 11th Int. Conf. Telecommun.*, Jun. 2011, pp. 211–218.

[26] Z. Xu, G. Xu, and Z. Zheng, "BER and channel capacity performance of an FSO communication system over atmospheric turbulence with different types of noise," *Sensors*, vol. 21, no. 10, p. 3454, May 2021. [Online]. Available: https://www.mdpi.com/1424-8220/21/10/3454

[27] A. L. Sanches, T. R. Raddo, J. V. dos Reis, and B.-H. V. Borges, "Performance analysis of single and multirate FFH-OCDMA networks based on PSK modulation formats," *J. Opt. Commun. Netw.*, vol. 7, no. 11, pp. 1084–1097, 2015.

[28] A. Jurado-Navas, J. M. G. Balsells, J. F. Paris, M. Castillo-Vázquez, and A. Puerta-Notario, "General analytical expressions for the bit error rate of atmospheric optical communication systems," *Opt. Lett.*, vol. 36, no. 20, p. 4095, Oct. 2011. [Online]. Available: https://opg.optica.org/ol/abstract.cfm?URI=ol-36-20-409
[29] J. M. Garrido-Balsells, A. Jurado-Navas, J. F. Paris, M. Castillo-Vázquez, and A. Puerta-Notario, "Spatially correlated gamma-gamma scintillation in atmospheric optical channels," *Opt. Exp.*, vol. 22, no. 18, pp. 21820–21833, Sep. 2014. [Online]. Available: https://opg.optica.org/oe/abstract.cfm?URI=oe-22-18-21820
[30] A. Bekkali, T. D. Pham, K. Kazaura, K. Wakamori, and M. Matsumoto, "Performance analysis of SCM-FSO links for transmission of CDMA signals under gamma-gamma turbulent channel," in *Proc. MILCOM IEEE Mil. Commun. Conf.*, Oct. 2009, pp. 1–5.
[31] A. Jurado-Navas, C. Á. Roa, M. Á. Roa, and M. Castillo-Vázquez, "Cooperative terrestrial-underwater wireless optical links by using an amplify-and-forward strategy," *Sensors*, vol. 22, no. 7, p. 2464, Mar. 2022, doi: 10.3390/s22072464.
[32] L. C. Andrews and R. L. Phillips, *Laser Beam Propagation Through Random Media*. Bellingham, WA, USA: SPIE, 2005.
[33] J. Garrido-Balsells, A. Jurado-Navas, J. Paris, M. Castillo-Vázquez, and A. Puerta-Notario, "On the capacity of M-distributed atmospheric optical channels," *Opt. Lett.*, vol. 38, no. 2, pp. 3984–3987, 2013.
[34] S. Bloom, E. Korevaar, J. Schuster, and H. Willebrand, "Understanding the performance of free-space optics," *J. Opt. Netw.*, vol. 2, pp. 178–200, Jun. 2003. [Online]. Available: https://opg.optica.org/jon/abstract.cfm?URI=jon-2-6-178
[35] M. A. Al-Habash, "Mathematical model for the irradiance probability density function of a laser beam propagating through turbulent media," *Opt. Eng.*, vol. 40, no. 8, pp. 1554–1562, Aug. 2001.
[36] A. Jurado-Navas, J. M. G. Balsells, J. F. Paris, and A. Puerta-Notario, "A unifying statistical model for atmospheric optical scintillation," in *Numerical Simulations of Physical and Engineering Processes*, J. Awrejcewicz, Ed. Rijeka: Intech-Open, 2011, ch. 8, pp. 181–206, doi: 10.5772/25097.
[37] A. Jurado-Navas and A. Puerta-Notario, "Generation of correlated scintillations on atmospheric optical communications," *J. Opt. Commun. Netw.*, vol. 1, no. 5, pp. 452–462, 2009.
[38] M. Alvarez-Roa, C. Alvarez-Roa, F. Fernandez-Aragon, T. Raddo, J. M. Garrido-Balsells, I. Tafur-Monroy, and A. Jurado-Navas, "Performance analysis of atmospheric optical communication systems with spatial diversity affected by correlated turbulence," *J. Opt. Commun. Netw.*, vol. 14, no. 7, pp. 524–539, Jul. 2022.
[39] V. A. Aalo, "Performance of maximal-ratio diversity systems in a correlated Nakagami-fading environment," *IEEE Trans. Commun.*, vol. 43, no. 8, pp. 2360–2369, Aug. 1995.
[40] M.-S. Alouini, A. Abdi, and M. Kaveh, "Sum of gamma variates and performance of wireless communication systems over Nakagami-fading channels," *IEEE Trans. Veh. Technol.*, vol. 50, no. 6, pp. 1471–1480, Nov. 2001.
[41] (2023). *Wolfram*. [Online]. Available: http://functions.wolfram.com/
[42] A. Goldsmith, *Wireless Communicatons*. Cambridge, U.K.: Cambridge Univ. Press, 2005.

MARÍA ÁLVAREZ-ROA received the B.Sc. and M.Sc. degrees in telecommunications engineering from the University of Malaga, Málaga, Spain, in 2021 and 2023, respectively. She is currently pursuing the Ph.D. degree with the Department of Electrical Engineering, Eindhoven University of Technology. She has been a Scholarship Researcher with the Department of Communications, University of Malaga. Her research interest includes wireless optical communications.

CARMEN ÁLVAREZ-ROA received the B.Sc. and M.Sc. degrees in telecommunications engineering from the University of Malaga, Málaga, Spain, in 2021 and 2023, respectively. She has been a Research Fellow with the Department of Communications, University of Malaga. Her research interest includes wireless optical communications.

THIAGO R. RADDO received the M.Sc. degree in electrical engineering from the University of São Paulo, São Carlos, Brazil, in 2012, and the Ph.D. degree in engineering sciences from Vrije Universiteit Brussel, Belgium, in 2017. He was a Visiting Researcher with the Technical University of Denmark, Denmark, in 2013. He was affiliated with the Faculty of Electrical Engineering and the Institute for Photonics Integration, Eindhoven University of Technology, Eindhoven, The Netherlands, where he contributed to multiple European research projects, including 5G-PHOS, 5G-MOBIX, CONCORDA, and QKD, in 2018. He was a Visiting Scholar with the Federal University of ABC, Brazil, in 2021. He is currently a Visiting Research Fellow with the University of Malaga, Málaga, Spain. He has also been a Consultant to the world's largest ICT companies for the last four years. He has coauthored more than 65 technical publications and contributed to the technical program of international conferences. His main research interests include 6G, THz, AI, photonic integrated circuits, free-space optics, and quantum communication. He is a member of OPTICA.

MIGUEL CASTILLO-VÁZQUEZ received the M.Sc. and Ph.D. degrees in telecommunication engineering from the University of Malaga, Spain, in 1997 and 2008, respectively. In 1997, he joined the Department of Communications Engineering, University of Malaga, where he is currently an Associate Professor. He is also a member of the Telecommunications Research Institute, University of Malaga. His research interests include indoor wireless optical communications, atmospheric optical communications, and smart satellite networks.

CARMEN CASTILLO-VÁZQUEZ received the M.Sc. and Ph.D. degrees in mathematics from the University of Malaga, Spain, in 1992 and 2001, respectively. In 1993, she joined the Department of Statistics and Operations Research, University of Malaga. She is currently an Associate Professor with the Eindhoven University of Technology. She is also a member of the Spanish Society of Statistics and Operations Research and the Telecommunications Research Institute, University of Malaga. Her research interests include Bayesian inference and statistical models in optical communications.

BEN-HUR V. BORGES received the Ph.D. degree in electrical engineering from Drexel University, Philadelphia, PA, USA, in 1997. From 1997 to 1998, he was a Postdoctoral Researcher with the São Carlos School of Engineering, University of São Paulo, São Carlos, Brazil. In 2005, he became an Associate Professor with the Department of Electrical and Computer Engineering, School of Engineering, University of São Paulo (SEL/EESC/USP). Since 2018, he has been a Full Professor with SEL/EESC/USP. His research interests include metamaterials and metasurfaces for microwave and optical applications, nanoplasmonics, the design and characterization of devices for communications and sensing applications, and the modeling of optical code multiple access networks. He is the Director of the Metamaterials Group: Microwave and Optics (GMeta) and an Editorial Board Member of the *Journal of Physics: Photonics*.

IDELFONSO TAFUR MONROY (Senior Member, IEEE) received the M.Sc. degree from the Bonch-Bruevich Institute of Communications, St. Petersburg, Russia, the Technology Licentiate degree in telecommunications theory from the Royal Institute of Technology, Stockholm, Sweden, and the Ph.D. degree from the Eindhoven University of Technology, Eindhoven, The Netherlands. He started the academic career with the Kharkiv Polytechnic Institute, Ukraine. He is the Director of the Photonic Integration Technology Center (PITC), The Netherlands, a Professor in photonics communication technologies with the Technical University of Denmark, Denmark, a Guest Professor with the Beijing University of Post and Telecommunications, Beijing, China, a Visiting Scientist with the University of California at Berkeley, Berkeley, CA, USA, and a Fellowship Professor with the ITMO University, St. Petersburg. He is currently a Professor with the Department of Electrical Engineering, Eindhoven University of Technology, leading the Quantum and Terahertz Systems Group. He is also the Co-Founder of the start-up Bifrost Communications on optical fiber access solutions. He is a Principal Investigator (PI) with the Center for Quantum Materials and Technology Eindhoven (QT/e), the Center for Photonics Integration (IPI), and the Center for Terahertz Science and Technology (CTST/e). He is also a PI with the CAT 2 Quantum Internet Project of the Dutch Quantum Delta Growth Fund. He has graduated 24 Ph.D. students. He is the coauthor of more than 500 journal and conference papers. His research interests include terahertz systems-on-chip, 5G and beyond systems, and converged electronic-photonic integrated circuits for applications in quantum, secure communications, sensing, and computing. He is a Senior Member of OSA.

ANTONIO JURADO-NAVAS (Member, IEEE) received the Ph.D. degree in telecommunication engineering from the University of Malaga, Málaga, Spain, in 2009. From 2002 to 2004, he was a Consultant with Vodafone-España. From 2009 to 2011, he was with the Department of Communications Engineering (Ingenieria de Comunicaciones), University of Malaga, as a Postdoctoral Researcher, where he became an Assistant Professor, in 2011. From 2012 to 2015, he was with Ericsson, where he was involved in geolocation tools for mobile networks. From 2015 to 2017, he was a Marie-Curie Fellow with the Technical University of Denmark, Denmark. In 2017, he joined the Eindhoven University of Technology to work for the Electro-Optical Communications Group as an Invited Researcher. Since 2018, he has been an Associate Professor with the Department of Communication Engineering, University of Malaga. He is currently the Vice-Dean for Students and Professional Development with the Telecommunications Engineering School, University of Malaga. His research interests include communication theory and wireless communications: free-space optical and satellite communications, terahertz systems, stochastic processes, wireless channel modeling, OCDMA, physical layer security, semantic communications, and efficient transmission techniques. From 2004 to 2008, he was a recipient of a Spanish Ministry of Education and Science Scholarship.